The Astrophysical Journal, 974:25 (21pp), 2024 October 10 https://doi.org/10.3847/1538-4357/ad7368

TIC 290061484: A Triply Eclipsing Triple System with the Shortest Known Outer Period of 24.5 Days

V. B. Kostov[1,2], S. A. Rappaport[3], T. Borkovits[4,5,6], B. P. Powell[1], R. Gagliano[7], M. Omohundro[8], I. B. Bíró[4,5], M. Moe[9], S. B. Howell[10], T. Mitnyan[5], C. A. Clark[11,12], M. H. Kristiansen[13], I. A. Terentev[14], H. M. Schwengeler[15], A. Pál[16], and A. Vanderburg[3]

[1] NASA Goddard Space Flight Center, 8800 Greenbelt Road, Greenbelt, MD 20771, USA
[2] SETI Institute, 189 Bernardo Avenue, Suite 200, Mountain View, CA 94043, USA; veselin.b.kostov@nasa.gov
[3] Department of Physics, Kavli Institute for Astrophysics and Space Research, MIT, Cambridge, MA 02139, USA
[4] Baja Astronomical Observatory of University of Szeged, H-6500 Baja, Szegedi út, Kt. 766, Hungary
[5] HUN-REN—SZTE Stellar Astrophysics Research Group, H-6500 Baja, Szegedi út, Kt. 766, Hungary
[6] Konkoly Observatory, Research Centre for Astronomy and Earth Sciences, H-1121 Budapest, Konkoly Thege Miklós út 15-17, Hungary
[7] Amateur Astronomer, Glendale, AZ 85308, USA
[8] Citizen Scientist, c/o Zooniverse, Department of Physics, University of Oxford, Denys Wilkinson Building, Keble Road, Oxford, OX13RH, UK
[9] Department of Physics & Astronomy, University of Wyoming, Laramie, WY 82072, USA
[10] NASA Ames Research Center, Moffett Field, CA 94035, USA
[11] Jet Propulsion Laboratory, California Institute of Technology, Pasadena, CA 91109, USA
[12] NASA Exoplanet Science Institute, IPAC, California Institute of Technology, Pasadena, CA 91125, USA
[13] Brorfelde Observatory, Observator Gyldenkernes Vej 7, DK-4340 Tølløse, Denmark
[14] Citizen Scientist, Planet Hunter, Petrozavodsk, Russia
[15] Citizen Scientist, Planet Hunter, Bottmingen, Switzerland
[16] Konkoly Observatory, Research Centre for Astronomy and Earth Sciences, MTA Centre of Excellence, Konkoly Thege Miklós út 15-17, H-1121 Budapest, Hungary

Received 2024 July 5; revised 2024 August 12; accepted 2024 August 21; published 2024 October 2

Abstract

We have discovered a triply eclipsing triple-star system, TIC 290061484, with the shortest known outer period, $P_{\rm out}$, of only 24.5 days. This "eclipses" the previous record set by λ Tauri at 33.02 days, which held for 68 yr. The inner binary, with an orbital period of $P_{\rm in} = 1.8$ days, produces primary and secondary eclipses and exhibits prominent eclipse timing variations with the same periodicity as the outer orbit. The tertiary star eclipses, and is eclipsed by, the inner binary with pronounced asymmetric profiles. The inclinations of both orbits evolve on observable timescales such that the third-body eclipses exhibit dramatic depth variations in TESS data. A photodynamical model provides a complete solution for all orbital and physical parameters of the triple system, showing that the three stars have masses of 6.85, 6.11, and 7.90 $M_{\odot}$, radii near those corresponding to the main sequence, and $T_{\rm eff}$ in the range of 21,000–23,700 K. Remarkably, the model shows that the triple is in fact a subsystem of a hierarchical 2+1+1 quadruple with a distant fourth star. The outermost star has a period of ~3200 days and a mass comparable to the stars in the inner triple. In ~20 Myr, all three components of the triple subsystem will merge, undergo a Type II supernova explosion, and leave a single remnant neutron star. At the time of writing, TIC 290061484 is the most compact triple system and one of the tighter known compact triples (i.e., $P_{\rm out}/P_{\rm in} = 13.7$).

Unified Astronomy Thesaurus concepts: Multiple stars (1081); Binary stars (154); Eclipsing binary stars (444); Close binary stars (254)

1. Introduction

Binary stars are ubiquitous in the Galaxy, with more than half of the Sun-like stars having a stellar companion, in many cases more than one (e.g., D. Raghavan et al. 2010; A. Tokovinin 2021, and references therein). In fact, the nearest star to the Sun—Proxima Centauri (R. T. A. Innes 1917)—is part of the α Centauri triple system (P. Kervella et al. 2017). The Proxima Centauri system is rather wide, and all three components are visually resolved. The inner binary, composed of α Centauri A and B, has an orbital period of nearly 80 yr, while Proxima takes about 550,000 yr to complete one orbit around the common center of mass. With an outer orbital eccentricity of about 0.5, the physical separation between the inner binary and the outer tertiary is about 4300 au at periastron and up to 13,000 au at apastron (P. Kervella et al. 2017). Quite a wide orbit indeed—Proxima Centauri is nearly 0.1 lt-yr closer to Earth than α Centauri A and B. Thus, it is perhaps unsurprising that it was not until recently that the triple nature of the system was demonstrated with high confidence (P. Kervella et al. 2017).

Triple-star systems cover an enormous range of physical parameters, stellar types, and orbital configurations. The long-period ones, like α Centauri, represent one end of the spectrum where the interactions between the individual components occur on such colossal timescales that a human observer is unlikely to witness an exciting event. By contrast, compact, short-period systems that reside at the other end of the spectrum of stellar triples can exhibit a multitude of detectable dynamical interactions, in many cases quite dramatic. Naturally, the shorter the outer period, the stronger the interactions between the individual components, such that the most interesting

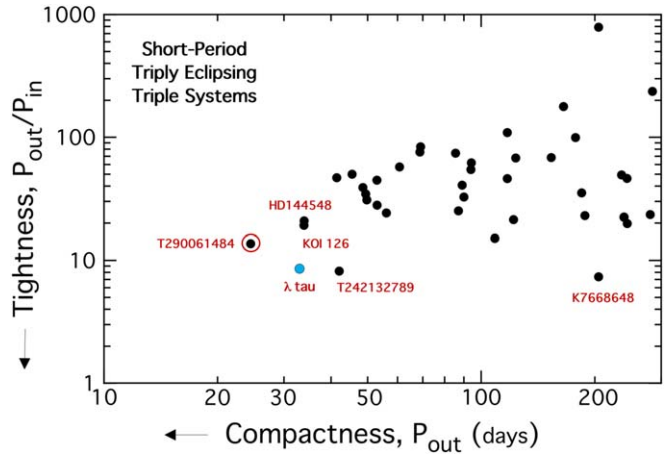

Figure 1. Tightness of triply eclipsing triple systems (P_{out}/P_{in}) as a function of the system compactness. λ Tau (marked by a blue symbol) is not triply eclipsing, but it is otherwise such a noteworthy benchmark system that we include it for reference. TIC 290061484, announced here and highlighted with a large open circle, is the most compact triple system known to date.

systems are usually those with outer orbital periods of less than 1000 days—typically referred to as compact hierarchical triples (CHTs; e.g., T. Borkovits et al. 2020; A. Tokovinin 2021).

CHTs that are also triply eclipsing, i.e., where the tertiary star eclipses, and is eclipsed by, the inner binary, are exceptionally valuable because they often enable a complete diagnosis of the system parameters. The stellar masses, radii, T_{eff}, and ages of these systems can be accurately determined, as can the complete set of orbital parameters, including the outer period and eccentricity and the mutual inclination angle. Remarkably, most of these can be estimated *without* radial velocity (RV) measurements. Instead, one can utilize various effects encoded in the information-rich eclipse timing variations (ETVs; i.e., light-travel time delays, dynamical delays, dynamically driven apsidal motion, and forced precession of the orbital planes) and in the timing and profile of the tertiary eclipses (e.g., T. Borkovits et al. 2020; S. A. Rappaport et al. 2022, 2023, 2024; T. Borkovits 2022, and references therein).

The technique of using such information from a multistellar object, coupled with a comprehensive "photodynamical" modeling analysis, was pioneered by J. A. Carter et al. (2011) for the case of the triple star KOI-126 found with Kepler. The model enabled subpercent-precision measurements of the masses and radii of the stars in KOI-126, which was particularly valuable for the M dwarfs of the inner binary. Compared to the relative handful of triply eclipsing triples that were known from the Kepler mission (T. Borkovits et al. 2016), TESS has already enabled the discovery of dozens of such systems (e.g., T. Borkovits et al. 2019a, 2020; S. A. Rappaport et al. 2022, 2023). These systems inform theoretical formation models indicating that such compact, and typically flat, multiples likely form and evolve differently compared to their wider counterparts (e.g., A. Tokovinin 2021; J. A. Docobo et al. 2021).

Yet, despite the large leap in the state of our knowledge of CHTs enabled by these discoveries, one thing had remained unchanged since the 1950s. For more than 68 yr, λ Tauri has reigned supreme as the CHT with the shortest outer period—33.02 days (E. G. Ebbighausen & O. Struve 1956). As highlighted in Figure 1, two systems came close to dethroning it—KOI-126 in 2011 (outer period of 33.92 days) and HD 144548 in 2015 (outer period of 33.95 days; R. Alonso et al. 2015). Two other CHTs were dynamically tighter (smaller P_{out}/P_{in}), but nothing came even close to pushing the record to much shorter outer periods.[17] Today, thanks to NASA's TESS mission, we were able to do so with the discovery and confirmation of TIC 290061484—a triply eclipsing CHT with an outer period of only 24.5 days, nearly 9 days shorter than that of λ Tauri.

This paper is organized as follows. In Section 2 we provide an overview of the system, outline the initial discovery, and discuss the observations. Section 3 presents a comprehensive photometric-dynamical solution of the system properties. We highlight the stellar and orbital properties of this system in Section 4, and we discuss our results in Section 5.

2. Discovery, Observational Material, and Preliminary Analysis

2.1. Discovery

We are continuously searching through the TESS full-frame image (FFI) photometry data for triple-star and higher-order multiple-star systems (see, e.g., T. Borkovits et al. 2020; S. A. Rappaport et al. 2022; T. Borkovits 2022; S. A. Rappaport et al. 2023, 2024; V. B. Kostov et al. 2024), generally following a three-stage process.

In the first phase, we download the FFIs from the Mikulski Archive for Space Telescopes (MAST). Then, with target lists assembled by using the `tess-point` (C. J. Burke et al. 2020) code on the TESS Input Catalog (TIC) to determine which sources are present in a given sector, we extract the light curves for stars with TESS magnitude $T \leqslant 15$ mag from the raw FFIs on the NASA Center for Climate Simulation *Discover* supercomputer[18] using the ELEANOR (A. D. Feinstein et al. 2019) code.

In the second phase, we use a neural network binary classifier trained to find eclipses in TESS light curves (see B. P. Powell et al. 2021a, 2022a; B. Powell 2022). The neural network preselects light curves that contain eclipses or features resembling eclipses for further visual examination. Generally, this process results in $\sim$1% of the total number of light curves being preselected, such that the fraction varies slightly depending on the density of stars in a particular sector (which causes blending of eclipses in the light curves of neighboring stars) and on systematic effects resembling eclipses. Thus, out of hundreds of millions of light curves that we have produced from TESS sectors 1–76 to date, this process has yielded "merely" a few million for further visual survey.

In the third phase of the search, our "Visual Survey Group" (VSG; M. H. K. Kristiansen et al. 2022) looks through these light curves by eye for extra eclipses that might indicate third-body eclipses in a 2+1 triple system, or extra sets of regular eclipses that could suggest another eclipsing binary (EB), potentially indicating a 2+2 quadruple system. In addition, the VSG searches for other unusual behavior associated with the EB such as pulsations that vary with the orbit (see, e.g., G. Handler et al. 2020). The visual surveying of the light curves is done with Allan Schmitt's `LcTools` and `LcViewer` software (A. R. Schmitt et al. 2019). This software makes it

[17] Importantly, tight triples are not necessarily compact triples. As pointed out by T. Borkovits (2022), the triple system LHS 1070 with $P_{out}/P_{in} = 88/18$ yr is close to the theoretical limit for dynamical stability—yet hardly compact.
[18] https://www.nccs.nasa.gov/systems/discover

Figure 2. TESS FITSH light curve of TIC 290061484. Each panel represents a different sector. The deep regular eclipses are from the 1.792-day inner EB. The tertiary eclipses are highlighted with red arrows. Note that the tertiary eclipse near day 2840 is difficult to see on this scale.

feasible to inspect a typical light curve in a matter of just a few seconds.

From our searches through EB light curves obtained thus far from the TESS observations, we have found more than 70 triply eclipsing triples (see, e.g., T. Borkovits et al. 2020; T. Mitnyan et al. 2020; T. Borkovits et al. 2022a; S. A. Rappaport et al. 2022; and S. A. Rappaport et al. 2023), over 200 eclipsing quadruples (V. B. Kostov et al. 2022, 2024), the first fully eclipsing sextuple-star system (B. P. Powell et al. 2021a), and other particularly unique systems (B. P. Powell et al. 2021b, 2022b). In this work we report the discovery of a new triply eclipsing triple-star system, TIC 20061484, with an outer orbital period of only 24.5 days—the shortest ever found by a wide margin. The inner binary period itself is 1.792 days. This is such an unusual system, including various kinds of interesting dynamical effects, that we report it separately here.

2.2. The TESS Light Curve and "Extra" Eclipses

TESS observed TIC 290061484 at a cadence of 1800 s in Sectors 15 and 16, 600 s in Sector 55, and 200 s in Sectors 56, 75, and 76 (K. G. Stassun et al. 2018). The basic parameters of the system are listed in Table 1. Once TIC 290061484 was noted by VSG as being special in the ELEANOR data, we extracted a somewhat improved light curve using the FITSH pipeline (A. Pal 2012), shown in Figure 2. The panels, arranged vertically, each represent a different TESS sector. The eclipses of the 1.792-day inner EB are readily apparent. In addition to these regular eclipses detected by the neural network, one of us (R.G.) noticed nine "extra" features (a couple of which are quite shallow) that do not belong to the EB. These are marked in the figure with red arrows, and their approximate times are listed in Table 2. Closer inspection of these events revealed that six of them occur with a spacing equal to an integer of ≈24.5 days, while the remaining three events follow the same implied underlying period, but phased by 0.37 periods (rather than midway between the other group). This indicated a triply eclipsing triple system where the outer orbit has an eccentricity of ∼0.2.

When we fit a linear ephemeris to the set of six eclipses mentioned above, we find a period of 24.489 days with a statistical uncertainty of 0.004 days. Of course, this did not immediately confirm the triple nature of TIC 290061484, as there is always the possibility that a second periodicity in an EB light curve might be due to another EB that is either physically related to the target (yet unresolved) or a resolved, unrelated field EB that accidentally contaminates the TESS aperture of the target. However, it was immediately clear that this is not the case for TIC 290061484 because (i) the shapes of the extra eclipses are quite asymmetric, (ii) one tertiary conjunction shows *two* extra eclipses separated by only

Table 1
Basic Parameters For TIC 290061484

Parameter	Value	Source
Identifying Information		
TIC ID	290061484	1
Gaia DR3 ID	2169382208774963072	2
α (J2000, deg)	316.109369	2
δ (J2000, deg)	51.225478	2
Gaia Measurements		
μ_α (mas yr^{-1})	−3.1094	2
μ_δ (mas yr^{-1})	−4.1678	2
ϖ (mas)	0.6147	2
RUWE	1.05	2
astrometric_excess_noise (mas)	0.12	2
astrometric_excess_noise_sig	5.13	2
non_single_star	0	2
$T_{\rm eff}$ (K)	15,392	2
Photometric Properties		
T (mag)	12.79	1
G (mag)	14.44	2
B (mag)	18.86	1
V (mag)	16.27	1
J (mag)	10.7	3
H (mag)	9.95	3
K (mag)	9.58	3
$W1$ (mag)	9.4	4
$W2$ (mag)	9.28	4
$W3$ (mag)	9.22	4
$W4$ (mag)	7.42	4

Sources: (1) TIC-8 (K. G. Stassun et al. 2018); (2) Gaia DR3 (Gaia Collaboration et al. 2021); (3) Two Micron All Sky Survey All-Sky Catalog of Point Sources (M. F. Skrutskie et al. 2006); (4) AllWISE catalog (R. M. Cutri et al. 2012).

Table 2
Approximate Times of Third-body Events[a]

Event	Primary[b]	Secondary[c]	Cycle[d]	Deviation[e]
1	8728.46	...	1.00	−0.33
2	8753.25	...	2.00	−0.03
3	9831.33	...	46.00	+0.54
4	...	9840.48	46.37	+0.58
5	10344.80	...	67.00	−0.25
6	...	10353.98	67.37	−0.18
7	10369.38	...	68.00	−0.16
8	...	10378.60	68.37	−0.05
9	10393.89	...	69.00	−0.13

Notes.
[a] Eyeball estimates only, due to the facts that the eclipses are asymmetric, sometimes incomplete, and not strictly periodic (i.e., they depend on the phasing of the inner EB near the times of the outer inferior and superior conjunctions). The uncertainty is on the order of 0.2 days.
[b] Times of the primary outer eclipses relative to BJD 2,450,000.
[c] Times of the secondary outer eclipses relative to BJD 2,450,000.
[d] The fractional cycle numbers account for the eccentricity of the outer orbit, $e_{\rm out} \simeq 0.2$.
[e] The deviations (in days) from a linear ephemeris with $P_{\rm out} = 24.489 \pm 0.004$ days.

≈0.4 days, and (iii) the ETVs in the 1.792-day EB, discussed below, have a nonlinear periodic structure with a period of 24.5 days.

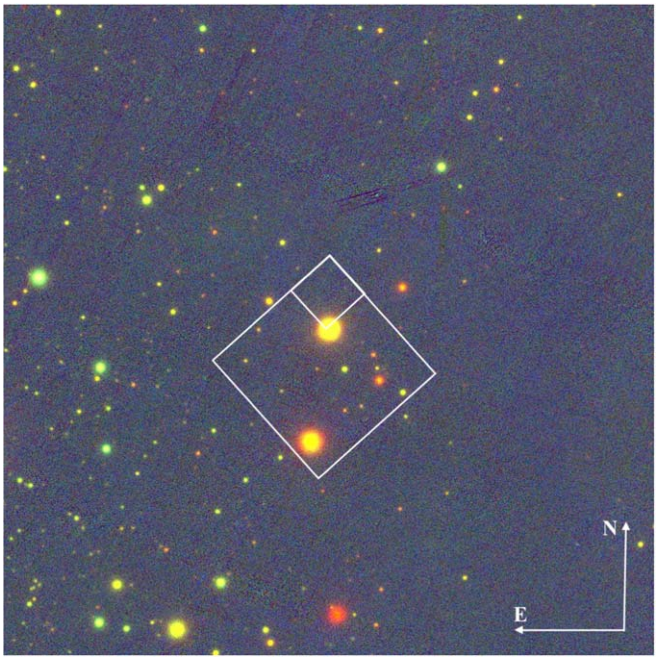

Figure 3. 4′ × 4′ PanSTARRS image (K. C. Chambers et al. 2016) centered on TIC 290061492. The small white contour represents one TESS pixel (21″ × 21″) oriented according to Sector 16, and the large white contour represents a 1′ × 1′ region. North is up, and east is to the left.

It is important to note that TIC 290061484 is rather close to the Galactic midplane ($b^{II} = 2.^\circ9$). A 4′ × 4′ PanSTARRS image of the region surrounding TIC 290061484 is shown in Figure 3. The nearest resolved star is TIC 290061492, at a separation of about 17″ and $\Delta m = 5.4$ mag (too faint to be the source of either the EB or the tertiary eclipses), while the nearest comparably bright source is TIC 290061506 at a separation of about 43.″8 and $\Delta m = 0.5$ mag. Thus, contamination in the TESS aperture of TIC 290061484 is quite low, and the observed eclipse depths represent the true depths. To pinpoint the origin of the eclipses, we performed two complementary tests: (i) a pixel-by-pixel analysis of the TESS light curve, and (ii) measurements of the center-of-light motion during the detected eclipses, using the methods described in V. B. Kostov et al. (2024, and references therein). Both tests confirm that the target is the source of the eclipses (see Figure 3).

2.3. Archival Data

To complement the TESS observations of TIC 290061484, we investigated the archival photometry from ASAS-SN (C. S. Kochanek et al. 2017), ATLAS (A. N. Heinze et al. 2018), and Zwicky Transient Facility (ZTF; M. J. Graham et al. 2019). There are insufficient ZTF observations to be useful for the purpose of tracking the outer eclipses. The ASAS-SN database contains 2350 observations, but the source is too faint ($G = 14.4$ mag) to detect even the 1.792-day EB. The ATLAS database contains 2800 observations. To analyze these, we first removed the eclipses of the inner binary by subtracting 50 harmonics of the 1.792-day eclipse structure and then subjected the cleaned data set to a box-fitting least squares (BLS) transform (G. Kovács et al. 2002) covering the period range 1–1000 days. The BLS analysis shows that the highest peak in the period range of 10–100 days occurs at a period of

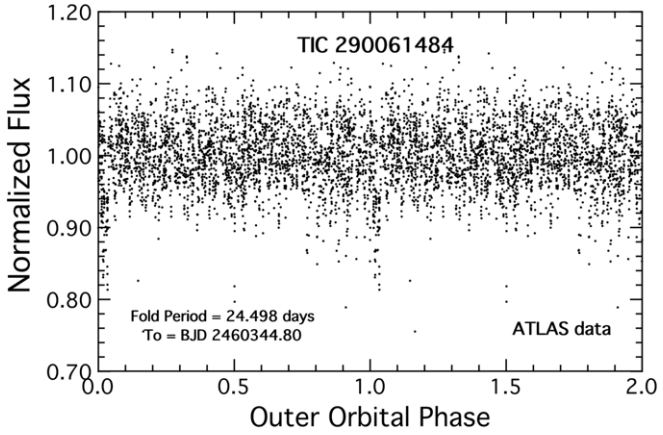

Figure 4. Point-wise fold of 2800 ATLAS archival data points for TIC 290061484. The fold period is 24.498 days, which represents the highest peak in the BLS transform for periods between 10 and 100 days. The eclipses of the inner binary have been removed prior to the BLS transform. Only one of the two outer eclipses appears (near phase 1.0), the other likely being smeared owing to the large jitter inherent in third-body eclipses that depend on both the inner and outer orbital phases. The uncertainty in the mean outer period from the ATLAS data alone is ±0.005 days.

24.498 ± 0.005 days. A point-wise fold of the cleaned ATLAS data about this period is shown in Figure 4.

We note that only one of the two sets of outer eclipses is detected in the ATLAS data. This is perhaps to be expected for the following reason. Even though there is a precise *underlying* outer period, the times of the outer eclipses are subject to substantial deviations from a linear ephemeris (of ∼half a day) because those eclipses depend not only on the outer orbital phase but also on the relative phases of the inner EB at the times of the superior and inferior outer conjunctions. Thus, it is perhaps not surprising that we are able to detect (weakly, at that) only one of the two sets of outer eclipses in the archival data.

3. Follow-up Observations of TIC 290061484

3.1. Ground-based Follow-up Observations

In order to extend the observational window for this remarkable triple system, we initiated photometric follow-up observations with the 80 cm RC telescope of Baja Astronomical Observatory, Hungary (BAO80), using a standard Sloan r'-band filter. The purpose of these observations is to (i) monitor the rapid, large-amplitude ETVs of the inner EB; (ii) detect expected third-body eclipses and refine the photodynamical solution; and (iii) characterize the prominent eclipse depth variations of both the inner and outer eclipses. By the time of submission of this manuscript we have just recorded one additional new third-body eclipse. The corresponding light curve was included in our detailed photodynamical analysis, as discussed below.

We note that the target is fairly faint ($V = 16.27$ mag) and obtaining RV measurements would be highly challenging. However, as discussed below, we are able to determine the parameters of the system without such measurements, and we also detail how this has been done numerous times in the past. Furthermore, it is important to point out that the key issue of the outer period of the triple, which is a major focus of this manuscript, does not depend in any way on RV measurements.

3.2. Speckle Interferometry

Additionally, to search for any wide companion in the TIC 290061484 system, we used the 'Alopeke high-resolution speckle imager mounted on the Gemini North 8 m telescope (N. J. Scott et al. 2021). 'Alopeke provides simultaneous speckle imaging in two bands of 562 and 832 nm. The output data products include reconstructed images in the two bands and robust contrast limits for companion detections. Twelve sets of 1000×0.06 s exposures, with an electron multiplying charge-coupled device (EMCCD) gain of 1000, were collected for TIC 290061484, as well as three sets of 1000×0.06 s exposures with an EMCCD gain of 10 for the point-spread function (PSF) standard star HR 8072. The PSF standard-star observations were taken immediately after TIC 290061484, and the observations were subjected to Fourier analysis in our standard reduction pipeline (S. B. Howell et al. 2011).

Figure 5 shows the reconstructed 832 nm image and resultant 5σ magnitude contrast limits obtained for the TIC 290061484 observations. TIC 290061484 was found to harbor no close companion stars of any significant flux within the range of the angular diffraction limit of $0\farcs02$ out to $1\farcs2$. At the distance to TIC 290061484 ($d = 1519$ pc) the angular limits correspond to spatial limits of 30–1822 au. The most stringent contrast limits achieved by the observations were 5–7 mag for the angular distance range $0\farcs1$–$1\farcs2$.

4. Photodynamical Modeling of the System

4.1. General Description of the Code

In order to extract all of the physical and orbital parameters of TIC 290061484, we utilized the software package LIGHTCURVEFACTORY (see, e.g., T. Borkovits et al. 2019a, 2020, and references therein). The code was developed to analyze multiple-star systems, including binaries, triples, and quadruple stars of both the 2+2 and 2+1+1 architecture. A detailed description of the inner workings of LIGHTCURVEFACTORY, the steps involved in the analysis procedure, and its application to a wide range of eclipsing multistellar systems can be found in T. Borkovits et al. (2018, 2019a, 2020, 2020) and T. Mitnyan et al. (2020, and references therein). Briefly, the code contains four main features: (i) emulators for multipassband light curve(s), the corresponding ETVs, and RVs (if available); (ii) an ability to calculate stellar masses (as proxies, in the absence of RV measurements), radii, temperatures, and several passband magnitudes (for fitting the net spectral energy distribution (SED) of the system) in an iterative manner, with the use of built-in PARSEC isochrone tables (C. T. Nguyen et al. 2022); (iii) a seventh-order Runge–Kutta–Nyström numerical integrator designed to calculate the perturbed 3D coordinates and velocities of all bodies in the system; and (iv) a Markov Chain Monte Carlo (MCMC)–based search routine for determining the best-fit system parameters and corresponding statistical uncertainties. The routine uses our custom implementation of the generic Metropolis–Hastings algorithm (see, e.g., E. B. Ford 2005).

Essentially all the details of how LIGHTCURVEFACTORY is used to analyze compact triply eclipsing triple systems discovered with TESS can be found in S. A. Rappaport et al. (2022). Here we provide only a high-level overview of the inputs to the code and of the parameters that are either fitted or constrained by the MCMC routine. Altogether, in the case of a hierarchical triple configuration, there are 25–27 system

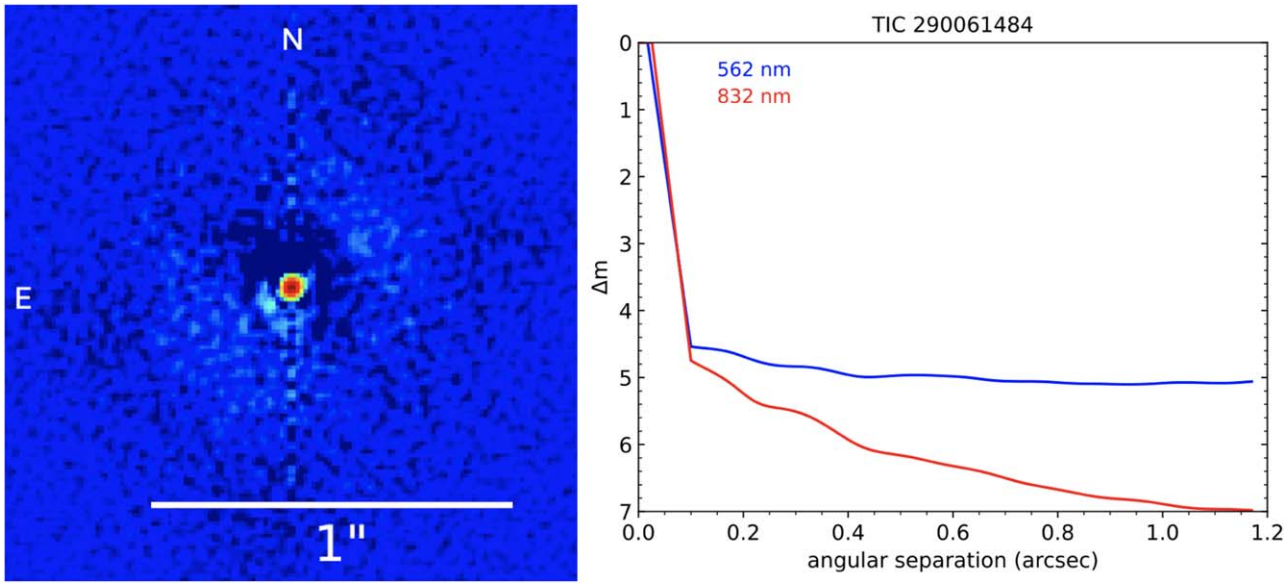

Figure 5. Contrast curves showing the 5σ magnitude limits for the 562 and 832 nm high-resolution speckle observations of TIC 290061484 Left: the reconstructed 832 nm image. Right: close companions can be excluded within 20 mas to 1.″2 of TIC 290061484 at the specified contrast limits.

parameters: (i) 9 stellar parameters (3 × mass, radius, $T_{\rm eff}$), (ii) 12 orbital parameters,[19] and (iii) 4 general parameters—distance, interstellar extinction, metallicity, and age. Finally, the code allows for passband-dependent contaminated (extra) light ℓ_4.

In turn, the input information can be broadly split into two basic categories. First, there are the "data" that include the (i) EB eclipse profiles, (ii) tertiary eclipse profile(s), (iii) eclipse times of the EB, (iv) archival SED values, and (v) RV measurements (not yet available for TIC 290061484). Second, we utilize PARSEC model stellar evolution tracks, isochrones, and atmospheres (C. T. Nguyen et al. 2022). The evolution tracks enable us to find the stellar radius and $T_{\rm eff}$ for a given stellar mass, age, and metallicity, while the isochrones allow us to compute stellar magnitudes in different passbands in order to fit the SED curve.

4.2. "Reader's Digest" Description of the Photodynamics Code

The entire photometric light curve and especially the eclipse fitting using the light-curve emulator for the inner binary yield dimensionless quantities such as $R_{\rm Aa}/a$, $R_{\rm Ab}/a$, and $T_{\rm Aa}/T_{\rm Ab}$, as well as $e_{\rm in}$, $\omega_{\rm in}$, and $i_{\rm in}$. Likewise, fitting of the outer eclipses yields another independent set of such ratios—and even more, as the profiles and timings of these outer eclipses are especially sensitive to more of the geometrical and dynamical quantities, including the mass ratios of both the inner and outer pairs, their mutual inclination, and so on. In the case of tight and compact systems, where the gravitational third-body interactions perturb the motions of all three stars on very short timescales (weeks and months), several further parameters can be inferred with great accuracy, including even the individual masses, which affect the timescales of such variations. This is especially true when both orbits are eccentric and the two orbital planes are inclined to each other, as is the case for TIC 290061484.

The SED fitting, given a Gaia distance, relates the absolute stellar radii and $T_{\rm eff}$ values to the composite system fluxes, which can be matched to the SED. In turn, for a given chemical composition, the stellar masses and system age are directly given by the radii and $T_{\rm off}$ values, and vice versa, via the stellar evolution tracks.

Finally, the ETV fitting from the binary eclipse timing, among other things, yields the same information as RV studies that would follow the gamma velocity of the binary; this measures the orbit of the binary center of mass around the tertiary star. But, in addition to that, there are other dynamical effects encoded in the ETV curve, e.g., which again determine such things as the eccentricity of both orbits, the orientation of the two orbits relative to each other and to the observer, and also both mass ratios. The latter effects are basically due to the way in which the tertiary star periodically alters the period of the inner binary. In most cases, the latter effect is unmeasureable with RV studies.

All these effects are extensively documented and verified in the various references given in Section 4.1.

4.3. Detailed Description of the Photodynamical Analysis of TIC 290061484

To model the light curve of TIC 290061484, we used the FFI FITSH photometry (A. Pal 2012). To save computational time, we binned the 200 and 600 s cadence data to 30-minute cadence,[20] and we only used the $\pm 0\overset{\rm p}{.}15$ phase-domain regions around the EB eclipses. However, whenever a data segment contains a third-body (i.e., "outer") eclipse, we keep the data for an entire binary period before and after the first and last contacts of that particular third-body eclipse.

We note that the lack of RV data does not prevent derivations of absolute stellar masses, temperatures, and radii. The light curve of a triply eclipsing triple contains a wealth of information that encodes combinations of the stellar masses. Additionally, the ETV curve

[19] In the case of available RV data, the systemic RV can be added as another parameter.

[20] While LIGHTCURVEFACTORY is able to handle directly finite exposure times, we found that finite exposure (more strictly speaking cadence) time corrections were unnecessary to apply even for the 30-minute-cadence light curves, due to the relatively long durations of both the inner and outer eclipses compared to the cadence times.

and (to a lesser extent) the light curve contain signatures of the dynamical delays that probe the mutual inclination and most of the inner and outer orbital elements.[21] In turn, these depend primarily on $q_{\rm out}$ and, through higher-order perturbations, on $q_{\rm in}$ (see, e.g., T. Borkovits et al. 2015). Additionally, the geometry and timing of the outer eclipses provide significant information about the ratio of $q_{\rm out}/q_{\rm in}$ (see Appendix A of T. Borkovits et al. 2013). The inner and outer eclipses constrain $R_{\rm Aa,Ab}/a_{\rm in}$ and $R_{\rm Aa,Ab,B}/a_{\rm out}$, respectively, and their combination leads to the abovementioned ratio of mass ratios.

To compensate for the lack of spectroscopically determined temperatures and metallicities, we combine SED-derived estimates of absolute temperatures (as employed by, e.g., N. J. Miller et al. 2020 and K. G. Stassun & G. Torres 2016) with the results of the simultaneous light-curve fits. The latter provide combinations of the ratios of the surface brightnesses and, hence, indirectly the absolute temperatures of the three stars. We note that the ratio of the surface brightnesses of the inner EB components can be obtained not only from the mutual eclipses of the inner components but also from the tertiary eclipses. Hence, from a light curve containing both inner and outer eclipses, the information that can be extracted is not simply the sum of the parameters that can be determined from two independent eclipsing light curves but much more.

Finally, we combine the SED information with theoretical, coeval stellar isochrones that provide information on the radii and $T_{\rm eff}$ of the stars (assuming that the three stars have the same age) and also on the masses for a given age.[22] And, of course, knowledge of the masses sets the size scales of the system, which then provides for absolute determinations of semimajor axes and stellar radii.

5. System Parameters

In the first stage of our analysis we searched for a photodynamical solution without the use of any additional astrophysical constraints such as the system SED or the use of PARSEC tables to constrain stellar masses, radii, and temperatures. In such a manner we have found some seemingly good solutions, but without very accurate information about the individual stellar masses and temperatures. Nonetheless, we were able to find good constraints on such dimensionless quantities as the mass and temperature ratios, as well as the fractional stellar radii.

We quickly realized, however, that our astrophysically unconstrained model was clearly unphysical, which led to the following problem. The two (robustly obtained) mass ratios of $q_{\rm in} = 0.89$ and $q_{\rm out} = 0.58$ revealed that the tertiary star should be more massive by $\approx$10% than the primary of the inner EB, and hence it is formally the most massive star in the triple, though not by much. Despite this fact, our solution resulted in a largely oversized tertiary star and, at the same time, substantially smaller, almost spherical stars for the inner binary.[23] Moreover, the tertiary star's effective temperature was found to be very close to that of the primary of the EB. At first glance, this apparent contradiction can be resolved by assuming that the tertiary star has just evolved off the main sequence (MS), while the EB's primary is still close to the zero-age MS (ZAMS). However, the problem with this interpretation is that we were unable to find a suitable combination of masses, ages, and metallicities that would have resolved all these contradictions. In other words, either the primary of the inner EB became too large, producing a more significant ellipsoidal light variation (ELV) on the light curve (in contradiction with the TESS observations), or the tertiary star was not large enough (and, moreover, it was too hot) for a satisfactory solution.

To resolve this issue, we employed two different strategies: (i) we allowed for the tertiary to be older than the two inner binary members and adjusted the age of the tertiary star independent of the age of the binary, and (ii) we allowed for a significant amount of extra light contamination of the system, which enabled a coeval solution.

Yet even after allowing for these two possibilities, a significant additional issue remained unresolved. Specifically, as one can notice in Figure 6, the medians of the TESS Year 2, 4, and 6 ETVs are offset relative to each other. The origin of such a period variation might be intrinsic (i.e., astrophysical), such as mass transfer between the binary components, mass loss, or some kind of magnetic effects (e.g., J. H. Applegate 1992). The physics of these phenomena and their mathematical form, as they are manifested in an ETV curve, are summarized in N. Nanouris et al. (2011, 2015). Such effects are less likely in the current system, due to the detached nature of the inner binary, as well as to the fact that these are hot stars and, thus, we do not expect strong magnetic fields. Therefore, in the current situation, it is more likely that the additional timing variations are caused by some extra dynamical effects. These might have arisen either (i) from some higher-order dynamical perturbations and, perhaps, some interactions between dynamical and tidally forced apsidal motion or, the simpler and more likely assumption, (ii) from the effect of an additional, more distant, fourth companion star.

First, we checked the former case. Satisfactory modeling of these effects, however, required very strong fine-tuning of the system parameters.[24] Hence, to make it easier for LIGHTCURVEFACTORY to find a satisfactory ETV solution, we allowed the code to adjust the first apsidal motion constant (k_2) for the two members of the inner binary. This solution resulted in $k_2^{Aa} = 0.022 \pm 0.002$ and $k_2^{Ab} = 0.006 \pm 0.003$. While the latter value is theoretically acceptable, the large value obtained for the primary star appears to contradict the models for such hot MS stars (see, e.g., A. Claret 2023).

Finally, however, we realized that we can obtain a much better ETV solution *and* resolve all the other problems discussed above, i.e., the large extra light contamination, the unphysical apsidal motion constant for the primary of the EB, and even the non-coeval evolution issue, by assuming that this extremely compact triple system is actually a subsystem of a quadruple system of (2+1)+1 hierarchy. In other words, we hypothesize that the system contains a fourth, somewhat more distant star, which (i) produces the missing flux ($\approx$20%–25% of the total flux) and, moreover, (ii) generates a light-travel time

[21] In general, the measured modulations in the ETVs also depend on the LTTE, which is equivalent to an SB1 RV measurement of the outer orbit. For the case of TIC 290061484, the LTTE is almost negligible relative to the dynamical delays.

[22] Naturally, such masses are no longer independent of astrophysical assumptions and, hence, may be somewhat inferior to those dynamical masses that can be directly inferred from high-quality RV data (see, e.g., T. Borkovits et al. 2020; T. Borkovits 2022).

[23] The latter finding comes from the fact that the inner EB exhibits only minor ELVs during the out-of-eclipse sections.

[24] Formerly, we have detected and successfully modeled the effects of such higher-order perturbations in the ETV curves of some tight and compact hierarchical triple and quadruple systems (T. Borkovits & T. Mitnyan 2023; T. Pribulla et al. 2023).

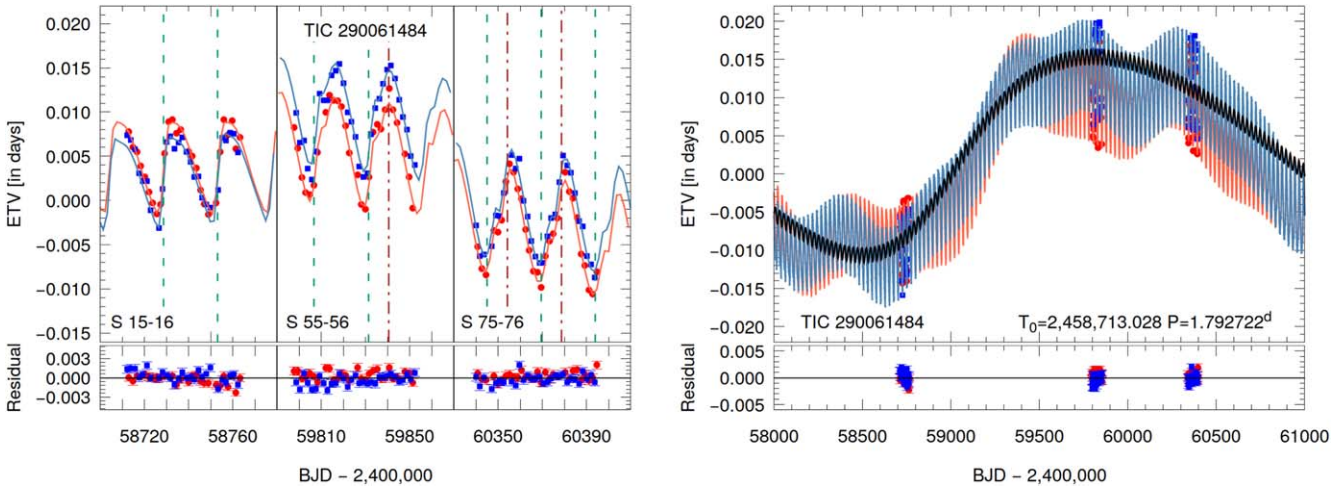

Figure 6. Left: primary and secondary ETVs of the inner binary constructed from the TESS FITSH data. The three panels each cover two sectors of TESS data (as labeled in the lower left corners), i.e., about two cycles of the outer orbit. Red (blue) points represent primary (secondary) eclipses. The smooth curves are model fits from the photodynamical analysis (see Section 4). The vertical dashed and dotted–dashed lines represent the locations of TESS observed eclipses where the binary eclipses the distant tertiary and vice versa, respectively. The lower panels represent the corresponding residuals. Right: same as the left panel, but zoomed out to cover an interval of about 8 yr. The black sinusoidal curve represents the pure LTTE contribution. This nicely illustrates that on a yearly timescale the ETV is chiefly dominated by the third-body perturbation effects (including the dynamically driven apsidal motion as well, but on a bit longer timescale, the LTTE, caused primarily by the fourth component, becomes dominant).

effect (LTTE; and, to a lesser extent, four-body perturbations) that may well explain the longer-term structure of the ETV curve. Hence, we switched LIGHTCURVEFACTORY into its (2+1)+1 quadruple-type mode, fixed the apsidal motion constants of the inner pair at a physically realistic value ($k_2^{(\mathrm{Aa,Ab})} = 0.01$), and reiterated the entire photodynamical analysis with these settings. The four-star model produced an excellent fit to all available data and indeed settled all the abovementioned issues associated with the initial three-star model.

In this regard, we note that it is not exceptional that a tight triple system has a more distant fourth stellar component as well. One example is the HIP 41431 system (T. Borkovits et al. 2019b), observed by the K2 mission. The tight triple nature of this system was identified independently via spectroscopic RV analysis of the three inner stars (with orbital periods of $P_{\mathrm{in}} = 2.9$ days and $P_{\mathrm{mid}} = 59$ days, respectively), as well as the ETV analysis of the innermost eclipsing pair. Then, historical RV measurements led to the certain discovery of a fourth component star on a wider orbit with a period of $P_{\mathrm{out}} = 3.9$ yr, the presence of which was also confirmed with follow-up eclipse timing measurements (T. Borkovits et al. 2019b).

In Table 3 we present the results for the system parameters (stellar and orbital) obtained from the photodynamical fit for this (2+1)+1 quadruple model. The following subsection discusses the results. The definitions of the parameters in Table 3 are listed in Table 4.

5.1. Discussion of the (2+1)+1 Quadruple Model Solution

Our results show that TIC 290061484 contains four massive stars: $M_{\mathrm{Aa}} = 6.85 \pm 0.15\,M_\odot$ and $M_{\mathrm{Ab}} = 6.11 \pm 0.15\,M_\odot$, representing the inner binary Aa+Ab; $M_{\mathrm{B}} = 7.90 \pm 0.27\,M_\odot$, representing the tertiary star B; and, bringing up the outer 2+1+1 configuration, the much more weakly constrained quaternary star C with $M_{\mathrm{C}} = 6.01 \pm 0.5\,M_\odot$. The corresponding stellar radii are not too far from the ZAMS, at $R_{\mathrm{Aa}} = 3.08 \pm 0.06\,R_\odot$, $R_{\mathrm{Ab}} = 2.80 \pm 0.06\,R_\odot$, $R_{\mathrm{B}} = 3.5 \pm 0.12\,R_\odot$, and $R_{\mathrm{C}} = 2.78 \pm 0.22\,R_\odot$. Not surprisingly, the stars are quite hot, with $T_{\mathrm{Aa}} = 22154 \pm 300$ K, $T_{\mathrm{Ab}} = 20877 \pm 400$ K, $T_{\mathrm{B}} = 23703 \pm 400$ K, and $T_{\mathrm{C}} = 20690 \pm 1000$ K. The system is young, at $t \approx 1.4 \times 10^7$ yr old.

We find a photometric distance to the system of $d = 1519 \pm 39$ pc with a very large color excess of $E(B-V) = 2.90 \pm 0.01$ mag, which leads to extreme extinctions, as $A_V \approx 7.9$ or, $A_G \approx 6.7$. Our distance is in essentially perfect agreement with the Gaia DR3–derived purely geometric distance of 1502 ± 41 pc (C. A. L. Bailer-Jones et al. 2021). In our interpretation, this result provides strong support for our quadruple system hypothesis.

The extreme extinction to this source, which is located near the Galactic midplane at $\ell^{II} = 91°$ and $b^{II} = 2\overset{\circ}{.}9$, makes the SED fitting difficult. As noted above, the photodynamical analysis indicates that $A_V \simeq 7.9$. This is at least qualitatively consistent with the hydrogen column density (to infinity) of $N_{\mathrm{H}} = 1.03 \times 10^{22}$ cm^{-2} provided by HEASARC.[25] Using a conversion factor of $N_{\mathrm{H}}(\mathrm{cm}^{-2}) \simeq 2.21 \times 10^{21} A_V$ (T. Güver & F. Özel 2009), we would estimate an A_V value that could be in the vicinity of 5.

TIC 290061484 has a significant mutual inclination of $i_{\mathrm{mut}} = 9\overset{\circ}{.}2 \pm 0\overset{\circ}{.}5$. As a natural consequence, both the inner and outer orbital planes precess with a (theoretical) period of $P_{\mathrm{node}} = 2.40 \pm 0.2$ yr. This means that the normal vectors of the inner and outer orbital planes (i.e., their orbital angular momentum vectors) move along the surfaces of cones with half-angles of $i_{\mathrm{in}}^{\mathrm{dyn}} = 8\overset{\circ}{.}5 \pm 0\overset{\circ}{.}4$ and $i_{\mathrm{out}}^{\mathrm{dyn}} = 1\overset{\circ}{.}77 \pm 0\overset{\circ}{.}05$ around the normal of the invariable plane of the whole triple subsystem (i.e., the net orbital angular momentum vector of the inner triple) with that period.[26]

The photodynamical model fits to the three segments of ETV results are shown in Figure 6. Each panel contains the ETVs from two adjacent sectors of TESS data, i.e., about 55 days in duration. Thus, the dominant nonlinear behavior will occur on the timescale of the orbital period of the inner triple, and

[25] https://heasarc.gsfc.nasa.gov/cgi-bin/Tools/w3nh/w3nh.pl?

[26] Here we consider the spin angular momenta of the three stars to be negligible.

Table 3
Orbital and Astrophysical Parameters from the Joint 2+1+1 Quadruple Photodynamical Light Curve, ETV, and SED and PARSEC Isochrone Solutions

	Subsystem		
	Aa–Ab	A–B	AB–C
Orbital Elements			
t_0 (BJD –2,400,000)	58711.0		
P[a] (days)	$1.79364^{+0.00013}_{-0.00013}$	$24.6347^{+0.0021}_{-0.0019}$	3205^{+140}_{-152}
a ($R_\odot$)	$14.59^{+0.11}_{-0.15}$	$98.18^{+0.68}_{-1.17}$	2734^{+102}_{-103}
e	$0.00250^{+0.00033}_{-0.00034}$	$0.2011^{+0.0022}_{-0.0024}$	$0.44^{+0.17}_{-0.18}$
ω (deg)	151^{+14}_{-12}	$92.2^{+2.1}_{-2.0}$	155^{+23}_{-23}
i (deg)	$85.50^{+0.27}_{-0.36}$	$94.43^{+0.15}_{-0.13}$	82^{+34}_{-22}
$\mathcal{T}_0^{\rm inf/sup}$ (BJD –2,400,000)	$58713.0340^{+0.0021}_{-0.0020}$	$58728.733^{+0.043*}_{-0.041}$	–
τ (BJD –2,400,000)	$58712.442^{+0.070}_{-0.059}$	$58704.228^{+0.165}_{-0.093}$	58931^{+78}_{-66}
Ω (deg)	0.0	$1.70^{+0.80}_{-1.02}$	-1^{+29}_{-17}
$(i_{\rm mut})_{\rm A-...}$ (deg)	0	$9.17^{+0.39}_{-0.42}$	29^{+17}_{-13}
$(i_{\rm mut})_{\rm B-...}$ (deg)	$9.17^{+0.39}_{-0.42}$	0	33^{+12}_{-18}
$\varpi^{\rm dyn}$ (deg)	332^{+14}_{-12}	$272.1^{+3.8}_{-2.9}$	334^{+22}_{-23}
$i^{\rm dyn}$ (deg)	23^{+15}_{-10}	27^{+11}_{-14}	$6.1^{+1.9}_{-3.1}$
$\Omega^{\rm dyn}$ (deg)	48^{+135}_{-109}	129^{+76}_{-160}	301^{+82}_{-157}
$i_{\rm inv}$ (deg)	84^{+28}_{-19}		
$\Omega_{\rm inv}$ (deg)	-1^{+23}_{-14}		
Mass ratio [$q = M_{\rm sec}/M_{\rm pri}$]	$0.890^{+0.015}_{-0.012}$	$0.610^{+0.012}_{-0.014}$	$0.288^{+0.019}_{-0.024}$
$K_{\rm pri}$ (km s^{-1})	$193.4^{+2.3}_{-2.6}$	$77.8^{+1.2}_{-1.8}$	$9.9^{+1.7}_{-1.7}$
$K_{\rm sec}$ (km s^{-1})	$217.1^{+2.1}_{-2.5}$	$127.4^{+1.1}_{-1.4}$	$35.3^{+4.4}_{-6.3}$
Apsidal and Nodal Motion Related Parameters			
$P_{\rm apse}$ (yr)	$2.75^{+0.15}_{-0.12}$	$15.60^{+0.14}_{-0.13}$	37124^{+53557}_{-14606}
$P^{\rm dyn}_{\rm apse}$ (yr)	$1.34^{+0.04}_{-0.04}$	$2.26^{+0.13}_{-0.18}$	3893^{+1651}_{-1124}
$P^{\rm dyn}_{\rm node}$ (yr)	$2.40^{+0.34}_{-0.14}$		4306^{+1224}_{-1502}
$\Delta\omega_{\rm 3b}$ (arcsec cycle^{-1})	4448^{+131}_{-134}	38660^{+3246}_{-2111}	2911^{+1195}_{-855}
$\Delta\omega_{\rm GR}$ (arcsec cycle^{-1})	$7.33^{+0.11}_{-0.15}$	$1.834^{+0.026}_{-0.043}$	$0.099^{+0.030}_{-0.011}$
$\Delta\omega_{\rm tide}$ (arcsec cycle^{-1})	296^{+18}_{-16}	$0.939^{+0.056}_{-0.053}$	$0.0016^{+0.0010}_{-0.0004}$

	Aa	Ab	B	C
Stellar Parameters				
Relative Quantities				
Fractional radius (R/a)	$0.2111^{+0.0030}_{-0.0028}$	$0.1922^{+0.0027}_{-0.0023}$	$0.0356^{+0.0009}_{-0.0010}$	$0.00102^{+0.00005}_{-0.00008}$
Temperature relative to $(T_{\rm eff})_{\rm Aa}$	1	$0.9426^{+0.0083}_{-0.0069}$	$1.0707^{+0.0100}_{-0.0116}$	$0.9351^{+0.0286}_{-0.0394}$
Fractional flux (in TESS band)	$0.2478^{+0.0054}_{-0.0059}$	$0.1866^{+0.0039}_{-0.0037}$	$0.3601^{+0.0253}_{-0.0222}$	$0.1804^{+0.0265}_{-0.0315}$
Fractional flux (in SLOAN r' band)	$0.2469^{+0.0065}_{-0.0092}$	$0.1843^{+0.0077}_{-0.0068}$	$0.3596^{+0.0296}_{-0.0236}$	$0.1779^{+0.0254}_{-0.0311}$
Physical Quantities				
M ($M_\odot$)	$6.853^{+0.151}_{-0.235}$	$6.106^{+0.142}_{-0.206}$	$7.903^{+0.234}_{-0.333}$	$6.009^{+0.399}_{-0.587}$
R ($R_\odot$)	$3.077^{+0.048}_{-0.045}$	$2.803^{+0.053}_{-0.050}$	$3.499^{+0.086}_{-0.113}$	$2.779^{+0.154}_{-0.215}$
$T_{\rm eff}$ (K)	22154^{+292}_{-407}	20887^{+362}_{-462}	23703^{+391}_{-472}	20690^{+615}_{-981}
$L_{\rm bol}$ ($L_\odot$)	2030^{+155}_{-128}	1339^{+122}_{-122}	3482^{+320}_{-417}	1271^{+305}_{-373}
$M_{\rm bol}$	$-3.50^{+0.07}_{-0.08}$	$-3.05^{+0.10}_{-0.09}$	$-4.08^{+0.14}_{-0.10}$	$-2.99^{+0.38}_{-0.23}$
M_V	$-1.29^{+0.05}_{-0.05}$	$-0.98^{+0.07}_{-0.05}$	$-1.70^{+0.10}_{-0.07}$	$-0.94^{+0.27}_{-0.17}$
$\log g$ (dex)	$4.295^{+0.011}_{-0.013}$	$4.327^{+0.009}_{-0.011}$	$4.248^{+0.018}_{-0.020}$	$4.331^{+0.026}_{-0.024}$

Global System Parameters	
log(age) (dex)	$7.116^{+0.092}_{-0.115}$
[M/H] (dex)	$-0.394^{+0.089}_{-0.066}$
$E(B-V)$ (mag)	$2.901^{+0.014}_{-0.013}$
Extra light $\ell_{\rm x}$ (in TESS band)	$0.018^{+0.031}_{-0.012}$
Extra light $\ell_{\rm x}$ (in SLOAN r' band)	$0.028^{+0.027}_{-0.019}$
$(M_V)_{\rm tot}$	$-2.77^{+0.06}_{-0.05}$
Distance (pc)	1519^{+39}_{-39}

Note.
[a] These are the instantaneous osculating periods, referred to time t_0. The long-term mean "observational" period for the triple is 24.498 ± 0.005 days.

Table 4
Definitions of the Parameters Listed in Table 3

Parameter[a]	Definition
t_0	Epoch time for osculating elements
P	Orbital period
a	Orbital semimajor axis
e	Orbital eccentricity
ω	Argument of periastron (of secondary)
i	Orbital inclination angle
$\mathcal{T}_0^{\rm inf/sup}$	Time of conjunction of the secondary[b]
τ	Time of periastron passage
Ω	Longitude of the node relative to the node of the inner orbit
$i_{\rm mut}$	Mutual inclination angle[c]
q	Mass ratio (secondary/primary)
$K_{\rm pri}$	"K" velocity amplitude of primary
$K_{\rm sec}$	"K" velocity amplitude of secondary
R/a	Stellar radius divided by semimajor axis
$T_{\rm eff}/T_{\rm eff,Aa}$	Temperature relative to EB primary
Fractional flux	Stellar contribution in the given band
M	Stellar mass
R	Stellar radius
$T_{\rm eff}$	Stellar effective temperature
$L_{\rm bol}$	Stellar bolometric luminosity
$M_{\rm bol}$	Stellar absolute bolometric magnitude
M_V	Stellar absolute visual magnitude
$\log g$	log surface gravity (cgs units)
[M/H]	log metallicity abundance to H, by mass
$E(B-V)$	Color excess in $B-V$ bands
Extra light, ℓ_4	Contaminating flux in the given band
$(M_V)_{\rm tot}$	System absolute visual magnitude
Distance	Distance to the source

Notes.
[a] The units for the parameters are given in Table 3.
[b] The superscript of "inf/sup" indicates inferior vs. superior conjunctions. (By default we give inferior conjunctions. Superior conjunctions are indicated by an asterisk.)
[c] More explicitly, this is the angle between the orbital planes of the inner binary and the outer triple orbit.

therefore there should be approximately two cycles in each panel. And, indeed, this is what we see. The semimajor axis of the EB orbit about the triple's center of mass is only about 33 $R_\odot$. Therefore, the classical LTTE will have an amplitude of only ∼0.0009 days. However, we can see from Figure 6 that the modulation amplitude of the ETV curves is nearly an order of magnitude larger. The explanation for this is that the ETV behavior is largely the result of dynamical delays caused by the varying distance of the EB to the tertiary star (see, e.g., S. Rappaport et al. 2013).

From the overall photodynamical fit, which includes the ETV curves as a major constraint on the system parameters, we find that the inner binary is nearly circular, with very small—but significant—nonzero eccentricity of $e_{\rm in} = 0.0025 \pm 0.0003$. This can be readily seen in the small, but varying, offsets of the secondary eclipses relative to a photometric phase of 0.5 (i.e., relative to the primary eclipses) in the three segments of the measured ETVs (Figure 6). This offset is a manifestation of the mainly third-body-forced, dynamical apsidal motion. As highlighted in the "Apsidal and Nodal Motion Related Parameters" section of Table 3, the tidally forced apsidal motion contribution is about 6%, and hence it is nonnegligible. In contrast, the relativistic contribution to the apsidal motion is nearly two orders of magnitude smaller and, thus, negligible. The theoretical net period of the apsidal motion is extremely short, $P_{\rm apse} = 2.8 \pm 0.1$ yr (see Table 3), and its effects are readily visible in the longer-timescale ETVs (Figure 6).

The most dominant property of the ETV curve on the longer timescales, however, is the abovementioned extra offset between the different years of TESS observations for which our fourth-body assumption provides a natural explanation. In Figure 6, besides the full photodynamical ETV solution for both the primary and secondary eclipses (red and blue, respectively), we also show the LTTE contribution caused by the orbit of the triple subsystem around the center of mass of the whole quadruple system (black curve). As one can see, on a timescale of a few years, this LTTE contribution will be the most characteristic effect. The corresponding parameters of the outermost orbit and the fourth, more distant component are also tabulated in Table 3.

With that said, we caution the reader that the *quantitative* results for the outermost orbit and fourth star are not very well constrained. There are several reasons for this caveat. First, an LTTE curve (which is what we are working with for the outermost orbit) does not contain any information about the spatial orientation of the orbital plane of the outermost orbit; hence, one can say nothing about its inclination and node. Likewise, one can say very little about the mutual inclination between any of the two orbits of the inner triple subsystem and the outermost orbit. In the current situation one can see that the median value for the mutual inclination between the middle and the outermost orbits is $(i_{\rm mut})_{\rm AB--C} = 29^\circ \pm 16^\circ$, which would result in a high-amplitude precession of the orbital plane of the inner triple subsystem. In turn, that would lead to the disappearance of the tertiary eclipses on a timescale of ∼10,000 tertiary orbits and even the binary eclipses after another ∼20,000 tertiary orbits. Such an outcome, however, is far from certain, and long-term monitoring would be needed to confirm or reject it.

It is important to note that some of the outermost orbital elements ($e_{\rm out}$, $\omega_{\rm out}$, and $\tau_{\rm out}$), as well as the outermost period $P_{\rm out}$, can be determined, at least in principle, with considerable accuracy from the ETV curve if at least one full cycle is observed. Naturally, the more cycles, the better the accuracy. Unfortunately, this is not the present case, as the available observations do not cover even a single outermost cycle.

Strictly speaking, in the current situation we cannot be certain even about the outermost period, not to mention all the other orbital elements. Despite this, as we have discussed in the previous section, we are quite certain about the presence of the fourth, more distant component. Hence, the (2+1)+1 configuration *qualitatively* seems fairly robust. Further observations will be critical to characterize the properties of the outermost subsystem with higher confidence.

With these cautionary remarks in mind, in what follows we briefly discuss the immediate observational consequences of our photodynamical solution concerning the inner triple subsystem, regardless of the presence and properties of an inclined fourth component.

The photodynamical model fits to the TESS light curves are shown in Figure 7. The asymmetric profiles of some of the tertiary events are readily seen, as well as their dramatic depth changes between the three TESS epochs (Sectors 15–16, Sectors 55–56, Sectors 75–76). The expected long-term light

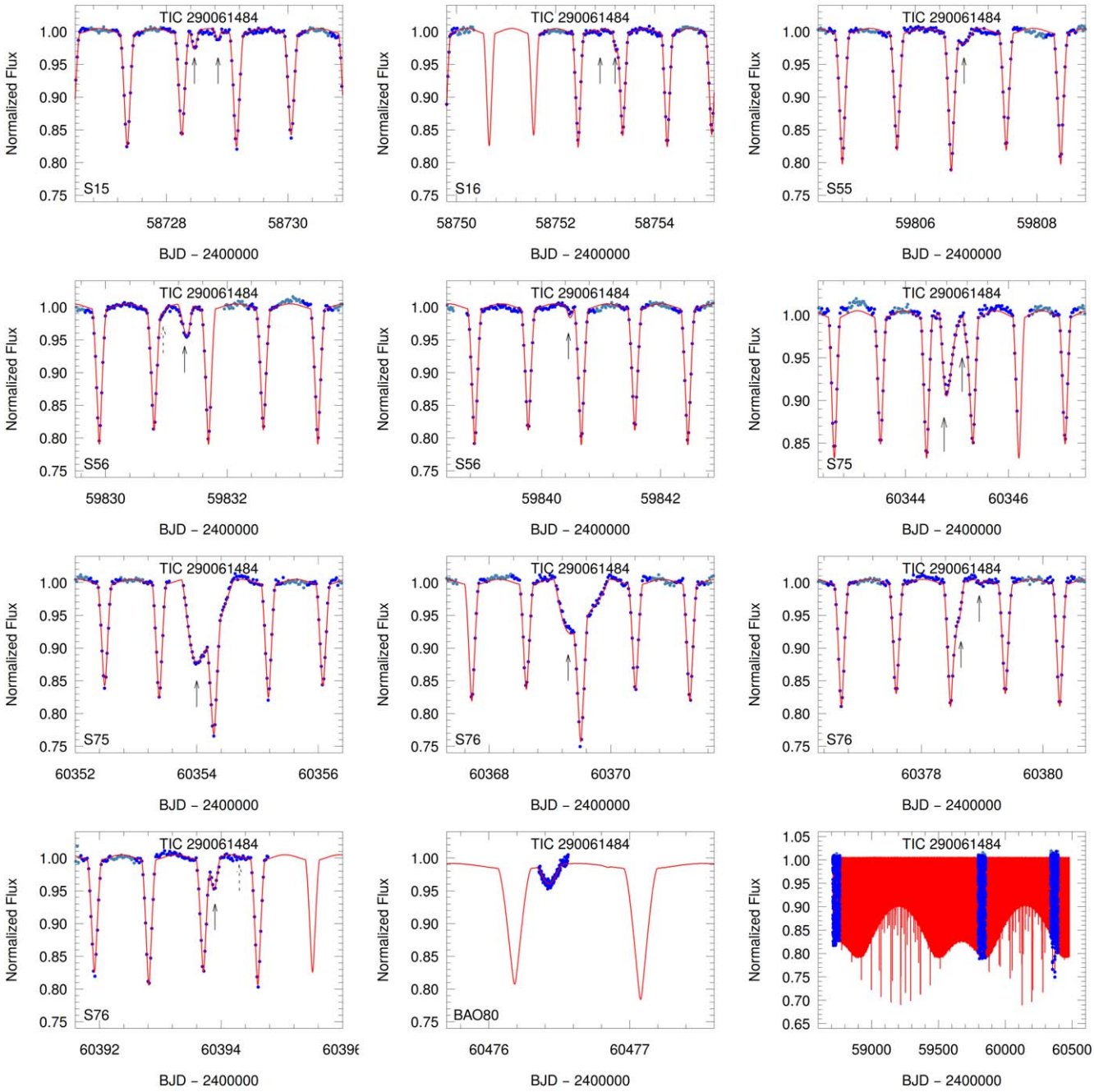

Figure 7. Panels 1–11, counting from top left: photodynamical model fits highlighting the tertiary eclipses of TIC 290061484 in Sectors 15, 16, 55, 56, 75, and 76. The blue points are the TESS photometric measurements, while the red curve is the model fit. The TESS sector is marked in the lower left corner of each panel. For an easier identification of the shallowest third-body eclipses, all tertiary events are marked with vertical arrows. Note that dashed arrows show two extremely shallow third-body eclipses that are present on the model light curve but cannot be identified in the observations. The middle panel in the last row presents the first tertiary event that has been detected in our ground-based photometric follow-up campaign, at BAO80. Bottom right panel: simulated long-term light curve of TIC 290061484 (red), emphasizing the expected eclipse depth changes. The dense pattern represents the EB eclipses; the thin lines extending below the pattern represent the tertiary eclipses.

curve of the system is shown in Figure 7, showcasing the changing eclipse depths of the inner binary due to the precession of its orbit.

The observable consequences of the orbital plane precession mentioned above and the corresponding periodic inclination variations are the *slightly* varying eclipse depths of the inner binary and the *substantially* varying depths and durations of the tertiary eclipses between the three TESS epochs (see Figure 7). Note, however, that besides the variations of the outer inclination, there is another effect that plays an important role in the duration and depth variations of the outer eclipses. This is the $P_{\rm apse,out} = 15.7 \pm 0.2$ yr period apsidal motion of the outer orbit. This effect results in a $\sim$120° variation of $\omega_{\rm out}$ during the $\sim$5 yr of the TESS observations (see Figure 8), which strongly influences the phase offsets, durations, and depths of the third-body eclipses.[27] Yet another aspect worth

[27] A nice illustration of the effects of the orientation of the apsidal line to the different properties of the eclipses can be seen in Figure 7 of T. Borkovits & T. Mitnyan (2023).

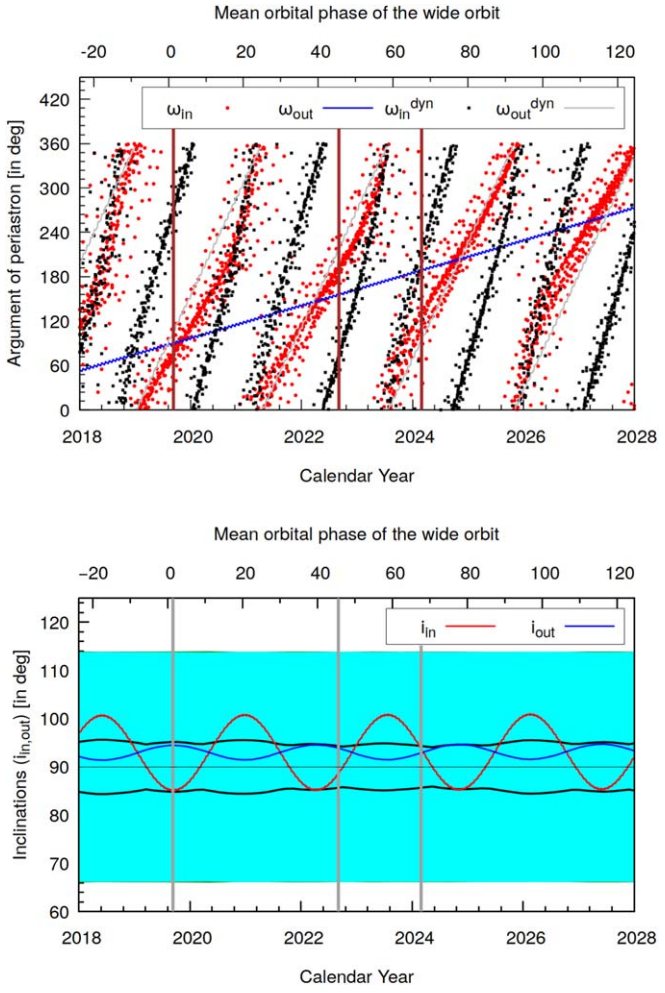

Figure 8. Top panel: the variations of the observable and dynamical arguments of periastron of the inner orbit (red and black circles, respectively), as well as the same orbital elements of the outer orbit (blue and gray curves). The vertical, thick gray lines represent the midtimes of the three segments of TESS observations. Bottom panel: the variations of the observable inclinations of both the inner and outer orbits (red and blue curves, respectively). The cyan area represents the domain of the (inner) inclination angle where regular, two-body eclipses may occur, while the two, mostly horizontal, thick black curves represent the borders of the third-body eclipses. As one can see, the inner inclination remains continuously well within its eclipsing domain; hence, the inner EB exhibits permanently deep eclipses. On the other hand, the outer inclination cyclically reaches, and even intersects, the border of the third-body eclipsing domain, which leads to very shallow, grazing, and even disappearing third-body eclipses from time to time.

noting is the different shapes of the ETV curves during the three epochs of the TESS observations (Figure 6). This is also the direct consequence of the apsidal motion of both orbits (and hence the variations in the parameters $\omega_{\rm in,out}$), which can be seen using the analytic formulae of T. Borkovits et al. (2015).

We are able to come full circle with the photodynamical modeling of the system by examining the system SED. In Figure 9 we show how the measured SED points from the blue out to the 10 μm Wide-field Infrared Survey Explorer 3 band, after correcting for the extreme interstellar extinction, are fit by model spectra for the four massive stars. In particular, we compare the dereddened SED points to theoretical passband magnitudes taken from the PARSEC isochrone grids. These are in substantial agreement. We also overlay the theoretical

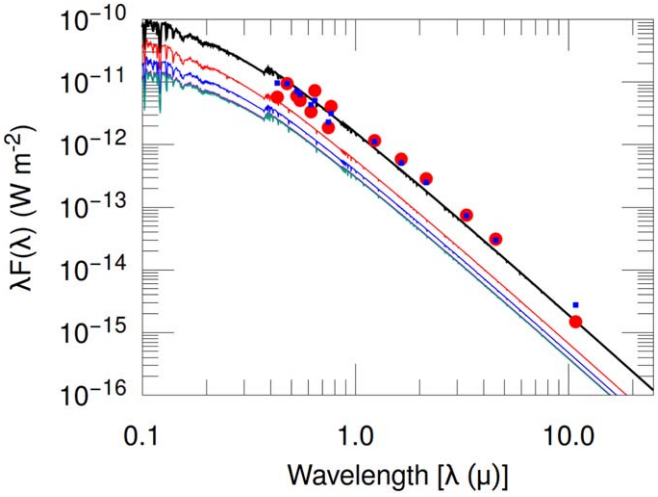

Figure 9. Cumulative SED of the TIC 290061484 system. Red circles represent the (dereddened) catalog passband magnitudes that were used in the SED fitting part of the joint photodynamical analysis. Blue squares stand for the theoretical passband magnitudes interpolated from the PARSEC isochrone grids. For comparison we plotted the theoretical ATLAS model atmosphere SEDs (F. Castelli & R. L. Kurucz 2003) for the entire system (thick black line representing the cumulative SED) and for the individual stars (thin red line: star B; thin blue line: star Aa; thin green line: stars Ab and C).

ATLAS model atmosphere SEDs of F. Castelli & R. L. Kurucz (2003), showing the contributions of the four individual stars and of the total system light.

Finally, we note that the sky-projected separation of the outermost orbit is $\sim$12 au. This is considerably smaller than the $\sim$30 au lower limit constraint achieved by the speckle imaging observations discussed above. Thus, while we cannot resolve the fourth star, at least we know that there is no fifth star present on an even wider orbit.

6. Summary and Discussion

6.1. System Properties

In this work we reported the discovery of a new triply eclipsing triple-star system, TIC 290061484, first detected in TESS data. The system is remarkable for several reasons. First, it has the shortest outer orbital period (24.498 ± 0.005 days, long-term average period) of any known triple-star system by quite a wide margin. Second, it has a low ratio of $P_{\rm out}/P_{\rm in} = 13.7$ and thus is highly dynamically interactive. Last but not least, the system exhibits many of the standard dynamical interactions, as well as several aspects that require follow-up observations and analysis for a more comprehensive understanding.

All of the system parameters, including those of all four stars and all three orbits, that we were able to derive from the photodynamical modeling are presented in Table 3.

6.2. Interesting Dynamical Interactions

Here we summarize the interactions that distinguish the TIC 290064184 triple system from others where the center of mass of the binary is in a simple, unperturbed, eccentric Keplerian orbit about the tertiary star. The triple system consists of a binary of total mass 13 $M_\odot$ in an eccentric orbit with a nearly 8 $M_\odot$ tertiary star. The triple's orbit has a mutual inclination angle (i.e., between the plane of the binary and that of the

triple) of ∼9° and an eccentricity of 0.2. The ETVs on the inner binary exhibit small LTTE delays and substantial dynamical delays with the period of the outer triple orbit of 24.5 days (see Figure 6). As discussed in Section 5.1, these dynamical delays are primarily due to physical changes in the binary period induced by the presence of the tertiary on its eccentric orbit. The dynamical delays have an amplitude of ∼9 minutes and vary in a quasi-sinusoidal manner. There is dynamically forced apsidal motion of the inner binary and outer triple orbits on timescales of ∼2.8 and ∼15.7 yr, respectively (see Section 5.1). A small but nonnegligible contribution to the binary's apsidal motion is from the classical tidal effect. There is also dynamically forced precession of the orbital planes on cones of half width 1.°8 and 8.°5 for the binary and outer triple orbit, respectively. The timescale for these precessions is ∼2.4 yr (see Section 5.1). These result in dramatic eclipse depth variations for the tertiary eclipses.

Dynamical simulations indicate that the EB eclipses will continue for millennia, while the tertiary eclipses will range from prominent to barely grazing on the same timescales (see Figures 7 and 8). The behavior of the eclipses on longer timescales depends on the still-uncertain configuration of the outermost orbit. For the best-fit photodynamical solution presented here, the EB eclipses do not stop, while the tertiary eclipses last for ∼30,000 outer periods, cease for the next ∼35,000 outer periods, and then start again.

The long-term ETV curve (see Figure 6) shows an LTTE variation of amplitude ∼18 minutes, which is unexplained in the context of the triple system. For this reason, among a couple of others related to the light curve and SED fitting, we invoked the presence of a fourth star in the system (in a 2+1+1 configuration) with an outermost period of ∼3300 days. With that, the model for the long-term ETV curve is fit very well.

Continuous monitoring of the ETVs might reveal some higher-order, smaller-amplitude perturbations that we have not yet explored. Especially interesting would be perturbations on the intermediate timescale between the outer orbit of less than a month and the longer-timescale apse-node perturbations.

6.3. Predictions of Future Eclipses

As one can see from Figure 6, the long-term ETV curve, dominated by the LTTE contribution of the orbit of the triple around the fourth star, is uncertain because of the relatively sparse sampling and a total observational baseline that is only ∼60% of the period of the outermost orbit (2730 days). Therefore, it would be extremely helpful to have continued ground-based follow-up observations of this object. Measured times of primary and secondary eclipses are always helpful, but the times of just a few third-body eclipses over the next couple of years will allow the photodynamical model to be updated in a meaningful way.

In Table 5 we list the midtimes of all 33 outer eclipses predicted by the photodynamics model for the next 500 days and deeper than $\Delta m \geqslant 0.1$ mag. Any observations of these eclipses would be very helpful, and we will update our photodynamics model accordingly as new eclipse times are provided.

The eclipse depths are also listed in Table 5. Two-thirds of the third-body eclipses are expected to be more than 5% deep, and these should be readily observable with amateur telescopes.

Table 5
Predicted Third-body Eclipse Events for the Next 500 Days

Midtime (BJD − t0)[a]	Width (deg)	Depth (Δ mag)	Midtime (BJD − t0)[a]	Width (deg)	Depth (Δ mag)
500.9	0.3	0.028	893.0*	0.1	0.136
549.9	0.2	0.011	893.1	0.3	0.135
697.3	0.2	0.017	907.4	0.1	0.014
746.0*	0.1	0.030	907.9	0.4	0.103
746.3	0.3	0.022	917.3	0.2	0.044
770.7	0.4	0.055	917.7	0.3	0.161
795.1	0.3	0.045	931.8	0.2	0.026
810.1	0.3	0.026	932.2	0.2	0.071
819.5*	0.1	0.053	941.7	0.3	0.078
819.7	0.4	0.075	942.1	0.2	0.101
834.5	0.2	0.036	956.1	0.3	0.034
843.8	0.2	0.022	956.8*	0.5	0.095
844.2	0.3	0.110	966.5*	0.9	0.209
868.3	0.2	0.032	981.2*	0.9	0.187
868.6	0.2	0.075	990.8	0.2	0.075
883.1*	0.1	0.068	991.2	0.4	0.191
883.4	0.5	0.097	…	…	…

Note.
[a] The reference time is −2,460,000; asterisks denote third-body events that are superposed with regular two-body eclipses.

6.4. Comparison with Previous Observations of Triples

Compared to the collection of 33 compact triply eclipsing triples discussed in S. A. Rappaport et al. (2024, see their Figure 22), TIC 290061484 stands out mostly for the substantially higher masses of its components, as well as the very short outer period. Most of the stellar masses in the systems discussed in S. A. Rappaport et al. (2024) are in the range of 1–3 $M_\odot$, with a typical value of ∼2 $M_\odot$. In contrast, the three stars in TIC 290061484 each have a mass above 6 $M_\odot$. Aside from that, the inner and outer mass ratios ($q_{\rm in}$ and $q_{\rm out}$) for TIC 2900661484 are consistent with those of the S. A. Rappaport et al. (2024) collection. Likewise, the outer orbital eccentricity of TIC 290061484 (0.2) is rather typical. The 9° mutual orbital inclination angle of TIC 290061484 is exceeded by only 3 of 33 systems discussed in S. A. Rappaport et al. (2024). As highlighted here, the outer orbital period is shorter, by far, than for any other triple system known at the time of writing.

We note that the other noteworthy close triple involving massive stars is TIC 470710327 (N. L. Eisner et al. 2022), where the inner and outer periods are 1.1 and 52 days, respectively. The system contains a tertiary of ∼15 $M_\odot$ and an inner binary of total mass ∼12 $M_\odot$. In this case, as a slight exception to the general rule that we have found for several dozen triples with less massive stars, TIC 470710327 has $q_{\rm out} \simeq 1.25 \pm 0.18$, i.e., marginally $\gtrsim$1. As discussed in N. L. Eisner et al. (2022), such massive stars are undoubtedly headed toward a Type II supernova during some future phase of the evolution of this system.

6.5. Searches for Triples with Even Shorter Periods

The discovery of TIC 290061484 with an outer orbital period of only 24.5 days, after the previously shortest period of 33 days (for λ Tau) had stood for 68 yr, raises the intriguing question of whether even more compact triple systems are possible. In order to have shorter outer periods, such systems

must (i) be able to form in the first place and (ii) be long-term dynamically stable.

To check the long-term dynamical stability of triple systems, which is a minimum requirement, we make use of the stability criteria for nearly coplanar triple systems summarized by S. Mikkola (2008). In particular, we use the formalism of R. A. Mardling & S. J. Aarseth (2001), expressed in terms of the orbital periods:

$$P_{\rm trip} \gtrsim 4.7\left(\frac{M_{\rm trip}}{M_{\rm bin}}\right)^{1/10}\frac{(1+e_{\rm out})^{3/5}}{(1-e_{\rm out})^{9/5}}P_{\rm bin}\ . \quad (1)$$

If we ignore the very weak dependence on mass and take $e_{\rm out}$ to be 0.2, as representative (and equal to the outer eccentricity in TIC 290061484), this expression comes to

$$P_{\rm trip} \gtrsim 7.8\,P_{\rm bin}\ . \quad (2)$$

For TIC 290061484, $P_{\rm out} = 13.66\,P_{\rm in}$, and thus the system should be long-term dynamically stable with room to spare. If we reduce both periods of TIC 290061484 in half, we would have a perfectly conventional 0.9-day inner binary and 12-day outer period, which is similarly stable. Even outer periods of 8–10 days seem not implausible to contemplate.

6.6. Formation Scenarios

Close binary companions cannot form in situ (A. P. Boss 1986; M. R. Bate 1998). Stellar companions instead fragment on protostellar disk or molecular core scales beyond $a > 10$ au and subsequently migrate inward, probably through circumbinary disk/envelope accretion whereby the orbital energy is dissipated into the surrounding gas (M. R. Bate et al. 2002; M. Moe & K. M. Kratter 2018; A. Tokovinin & M. Moe 2020; S. S. R. Offner et al. 2023). Extremely compact triples likely form through a specific sequence of two fragmentation episodes and substantial circumbinary/triple accretion. Circumtriple accretion tends to dampen the eccentricities and reduce the mutual inclination of the orbits (M. R. Bate et al. 2010; M. R. Bate 2012), which are necessary ingredients in maintaining dynamical stability while hardening toward an extremely compact configuration (see above).

Moreover, as a binary migrates inward, most of the mass from the circumbinary disk is accreted by the companion, thereby driving the mass ratio toward unity (B. D. Farris et al. 2014; M. D. Young & C. J. Clarke 2015). Close solar-type binaries exhibit an excess of twins with $q = 0.96$–1.00 (A. A. Tokovinin 2000; M. Moe & R. Di Stefano 2017; see Figure 14 in K. El-Badry et al. 2019) and a deficit of $q < 0.1$ companions known as the brown dwarf desert (D. Grether & C. H. Lineweaver 2006). Toy models of disk fragmentation, inward disk migration, and circumbinary disk accretion can successfully reproduce the observed brown dwarf desert and measured 25% twin fraction within $P < 100$ days (A. Tokovinin & M. Moe 2020).

An ultracompact triple like TIC 290061484 with $P_{\rm out} = 24.6$ days requires a delicate, fine-tuned, multistaged formation process. If the companions fragment too late, the remaining gas in the surrounding disk/envelope would be insufficient to harden the components. Conversely, if the inner binary undergoes inward disk migration that is too efficient, the pair will merge during the pre-MS. Similarly, if the tertiary migrates inward too quickly relative to the inner binary, the triple can become gravitationally unstable (see Equation (1)), which typically results in the least massive component being thrown to large separations or ejected entirely (M. Valtonen & H. Karttunen 2006; M. Moe & K. M. Kratter 2018).

We compile a list of 44 compact triples with $P_{\rm out} < 300$ days and measured component masses, including the triply eclipsing triples in Figure 1 and slightly misaligned triples that have noneclipsing tertiaries (T. Borkovits et al. 2022b; B. P. Powell et al. 2022b; N. L. Eisner et al. 2022; P. Gaulme et al. 2022; J. A. Orosz 2023; T. Borkovits & T. Mitnyan 2023; A. Moharana et al. 2024, T. Borkovits et al., 2024, in preparation). We exclude λ Tau because the inner binary is an evolved, semidetached Algol that has widened its orbit as the subgiant donor has transferred most of its mass to the MS accretor. We count nine extremely compact triples with $P_{\rm out} < 50$ days, of which eight have $P_{\rm in} = 0.8$–1.8 days, including TIC 290061484 (the single exception is TIC 2421327789 with $P_{\rm in} = 5.1$ days). Most extremely compact triples therefore have inner binaries that migrated to extremely close separations while narrowly avoiding a merger. In particular, the inner binary of TIC 290061484 contains early-type components, currently $R = 3\,R_\odot$ but likely $R \approx 5\,R_\odot$ during the embedded pre-MS phase, and thus just barely escaped overfilling its Roche lobe.

It should be noted that 96% of very close binaries with $P < 3$ days are in triples (A. Tokovinin et al. 2006). It was originally speculated that the tertiary played an active role in hardening the inner binary via Kozai–Lidov cycles and tidal friction (L. G. Kiseleva et al. 1998; D. Fabrycky & S. Tremaine 2007). However, M. Moe & K. M. Kratter (2018) demonstrated that most triples do not have the necessary orbital configurations to dynamically harden the inner binary to very short periods. Moreover, the timescales of dynamical hardening and tidal friction are too long to reproduce the observed population of young pre-MS binaries with $P < 3$ days, and thus they concluded that most very close binaries must derive from inward migration in a gaseous disk/envelope during the pre-MS phase. A. Tokovinin & M. Moe (2020) subsequently explained the common origin responsible for the observed correlation between very close binaries and their large triple-star fraction. The formation and migration of a binary to very short periods require a massive disk/envelope, and such a massive disk/envelope is also more likely to fragment twice, thereby forming a triple. Similarly, the formation and migration of an ultracompact triple like TIC 290061484 required an even more massive disk/envelope, which was prone to fragment into the compact 2+1+1 quadruple that we see today.

The average mutual inclination of triples/quadruples increases with increasing separation (A. Tokovinin 2017a). The outer component in TIC 290061484 is probably more misaligned than the ultracompact triple. In fact, given the measurement uncertainties in our photodynamical fit (see Table 3), the quaternary could conceivably have a sufficiently large mutual inclination $i_{\rm mut} > 39^\circ$ to excite Kozai–Lidov cycles in the tertiary, potentially responsible for its 9° misalignment with respect to the inner binary. However, the outer component cannot be so inclined to cause substantial pumping of the tertiary's eccentricity. The tertiary must remain below $e < 0.38$ to remain dynamically stable according to Equation (1), and thus the outer component must have $i_{\rm mut} \lesssim 45^\circ$ (quadrupole-order approximation; Equation (20) in S. Naoz 2016).

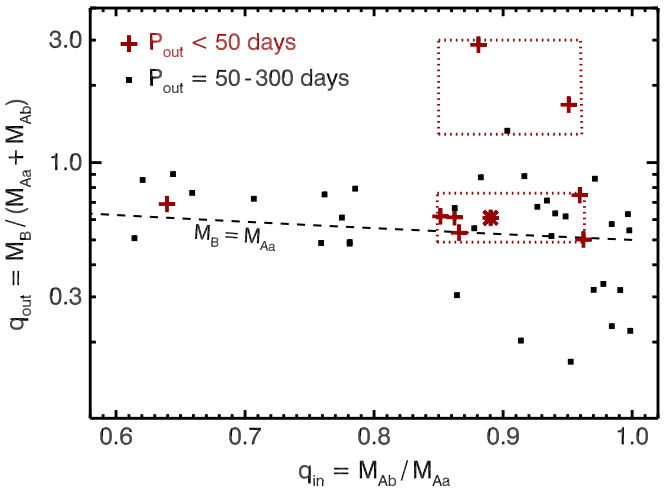

Figure 10. Outer vs. inner mass ratios for compact triples with $P_{\rm out} < 300$ days. We highlight the nine extremely compact triples with $P_{\rm out} < 50$ days (red plus signs), including TIC 290061484 (red asterisk), and we bracket their two main islands (dotted red lines). A triple where the tertiary is the most massive component lies above the dashed line.

The unique channel of circumtriple accretion that hardens a triple to below $P_{\rm out} < 50$ days imprints a unique signature on its mass ratios $q_{\rm in} = M_{\rm Ab}/M_{\rm Aa}$ and $q_{\rm out} = M_{\rm B}/(M_{\rm Aa} + M_{\rm Ab})$. In Figure 10, we display the inner and outer mass ratios for our 44 triples with $P_{\rm out} < 300$ days and measured component masses (two with $q_{\rm in} < 0.45$ fall off the plot because they are to the left of the displayed domain). Of our nine extremely compact triples with $P_{\rm out} < 50$ days, all but one (TIC 332521671) have inner mass ratios that span a narrow interval $q_{\rm in} = 0.85$–0.96. The inner binaries are relatively near equal mass but not quite true twins. As discussed in A. Tokovinin & M. Moe (2020), twins must have initially fragmented early in their formation process and experienced significant circumbinary disk accretion. Of our 44 triples with $P_{\rm out} < 300$ days, 9 (20%) have $q_{\rm in} > 0.96$, consistent with the observed 25% twin fraction among all very close solar-type binaries. The components of the inner binaries in extremely compact triples must have also fragmented relatively early and experienced substantial circumbinary disk accretion to exceed $q_{\rm in} > 0.85$. However, the presence and hardening of the compact outer tertiary interrupted the final accretion toward twin status, and thus extremely compact triples have inner binaries that mostly span $q_{\rm in} = 0.85$–0.96.

The majority (7/9) of the extremely compact triples have $q_{\rm out} = 0.50$–0.75. As a low-mass tertiary migrates inward and accretes most of the mass from the circumtriple disk, the outer mass ratio increases. Just as there is a desert of close brown dwarf companions below $q < 0.1$, there is a desert of tertiaries below $q_{\rm out} < 0.5$ within $P_{\rm out} < 50$ days. Conversely, it is more difficult to harden a companion that is already a twin. In the A. Tokovinin & M. Moe (2020) model, most of the inward disk migration occurs when $q < 0.2$, and the migration halts once the companion accretes to $q = 1$. It is thus not surprising that all known triples with $q_{\rm out} = 0.75$–1.0 have tertiaries that remain beyond $P_{\rm out} > 50$ days.

Disk fragmentation, inward migration, and circumtriple disk accretion can only form triples with $q_{\rm out} < 1$ (A. Tokovinin & M. Moe 2020), and indeed the majority of compact triples have $q_{\rm out} < 1$. The three outliers with massive tertiaries spanning $q_{\rm out} = 1.3$–3.0 in Figure 10 are KOI-126, HD 181068, and TIC 470710327. The latter has an outer tertiary with $P_{\rm out} = 52$ days, marginally wider than our extremely compact triples arbitrarily defined as those with $P_{\rm out} < 50$ days. These three systems mirror the main population of extremely compact triples but with inverted outer mass ratios, i.e., the inner binary components are similar in mass with $q_{\rm in} = 0.85$–0.96, suggesting significant circumbinary disk accretion. The outer pairs of these three systems with $q_{\rm out} > 1$ likely formed via core fragmentation. Both KOI-126 and TIC 470710327 have modest outer eccentricities $e_{\rm out} = 0.3$, further indicating a dynamical origin whereby the tertiary fragmented on larger core scales.

A larger sample of compact triples with $q_{\rm out} > 1$ is needed to better understand their formation. Fortunately, our main island of extremely compact triples, including TIC 290061484, is better constrained. Circumbinary accretion hardened the inner binary to $P_{\rm in} = 0.8$–1.8 days and $q_{\rm in} = 0.85$–0.96, and circumtriple accretion hardened the tertiary to $P_{\rm out} < 50$ days and $q_{\rm out} = 0.50$–0.75, all while maintaining dynamical stability and avoiding a merger of the inner binary.

In Appendix B we simulate the formation of a very large population of multistellar systems, and we show that there is only one ultracompact triple like TIC 290061484 for every ∼1.3 million star systems. We also estimate that for every triple like TIC 290061484 that could successfully thread the needle of migrating to $P_{\rm out} = 25$ days while maintaining dynamical stability, there were likely 10^4 triples that became disrupted during their formation process.

6.7. Long-term Dynamical Stability

Based on the analytic fitting formulae for long-term dynamical stability in triple systems (see Equation (1)), the triple subsystem of TIC 290061484 has a ratio of $P_{\rm out}/P_{\rm in}$ that is nearly twice that required for stability (∼13.7 vs. 7.8). The outermost orbit is comfortably stable as well, with a ratio of $P_{\rm out}/P_{\rm in}$ that is more than seven times larger than the minimum allowed ratio of ∼18.6.

For completeness, we numerically integrated the orbits of TIC 290061484 over the next 1 million years (∼15 million outer orbits), utilizing the REBOUND N-body code (H. Rein & S.-F. Liu 2012), utilizing REBOUNDX for the treatment of tidal effects (D. Tamayo et al. 2020), and using the best-fit parameters from the photodynamical solution as initial conditions at the reference time. The configuration of the system as seen from above is shown in the top panels of Figure 11 for 1, 10, 100, and 1000 outer orbits (∼25, ∼250, ∼2500, and ∼25,000 days, respectively), showcasing the relatively rapid precession of the inner and outer orbits.

The dynamical evolution of the system's orbital parameters over the course of 100,000 outer orbits is shown in the bottom panels of Figure 11. The inner and outer semimajor axes oscillate by no more than ∼1.5% and ∼0.7%, respectively. The eccentricity of the inner/outer orbits does not exceed ∼0.03/0.21, respectively. As seen from the figure, the most notable oscillations are in the inner and outer inclinations, where the former varies by up to ∼32° (i.e., from 68° to 100°). Overall, the simulations demonstrate that, indeed, the orbital architecture of the system remains largely unchanged, without any indications for chaotic motion for the duration of the numerical integrations.

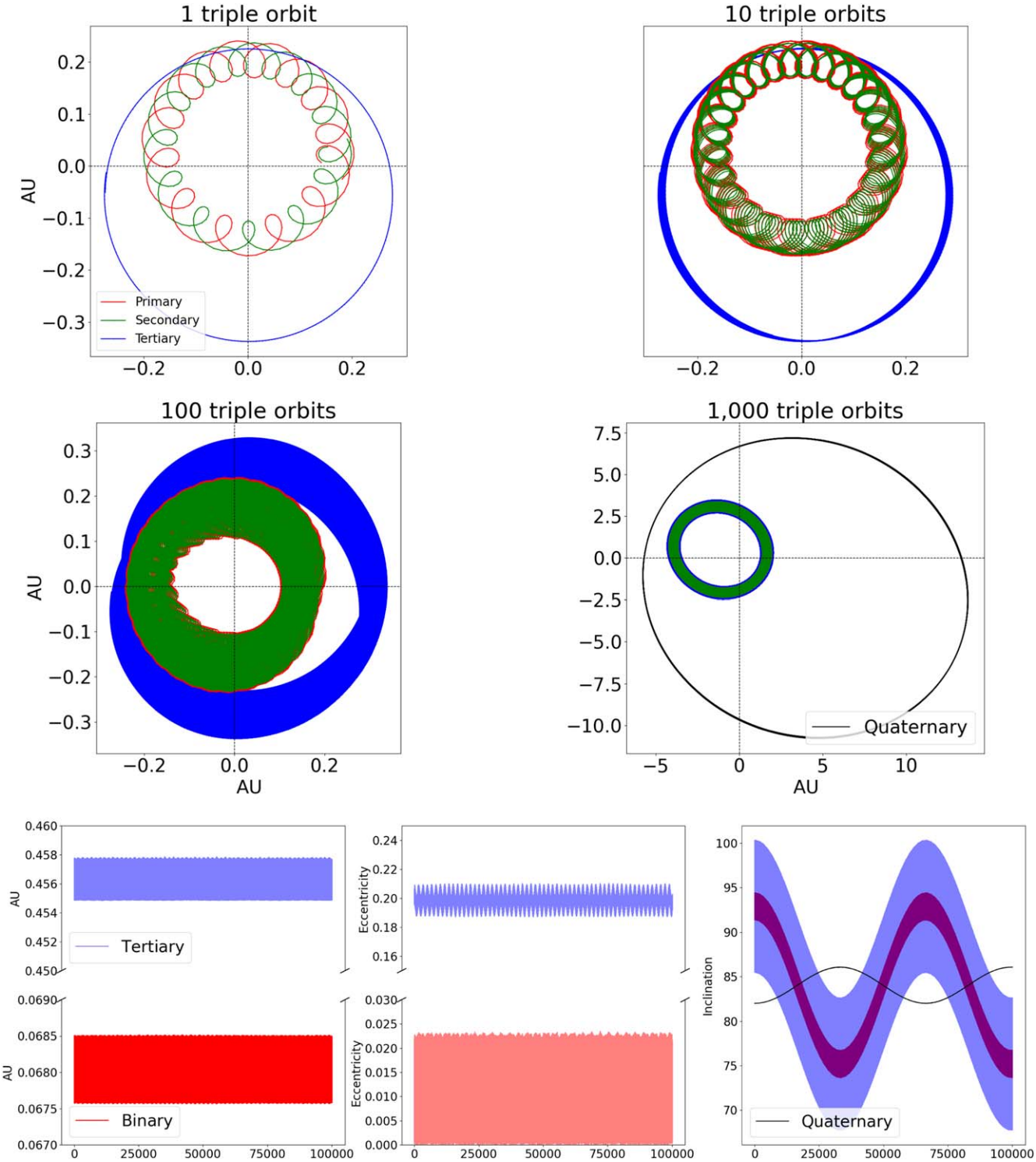

Figure 11. Top and middle panels: orbital configuration of TIC 290061484 as seen from above the outer orbital plane over the course of 1, 10, 100, and 1000 triple orbits (top left, top right, middle left, and middle right panels, respectively). The individual components are color-coded as indicated in the legend. The observer is in the *x*-*y* plane, looking along the *y*-direction. To highlight the rapid orbital precession of the triple subsystem, the top left, top right, and middle left panels are shown in the center-of-mass reference frame of that system. The middle right panel is shown in the center-of-mass reference frame of the entire quadruple system. Bottom panels: dynamical evolution of the system over the course of 100,000 triple orbits (∼2.5 million days) showing the semimajor axes (left), eccentricity (middle), and inclination (right) for the inner binary (red) and for the outer tertiary (blue). The parameters are plotted once a day for viewing purposes. There are no indications for chaotic motion, and the system is dynamically stable for the duration of the integrations.

6.8. Future Evolution of the TIC 290061484 System

Currently, star B fills some 11% of its Roche lobe in the outer orbit of the triple, while star Aa fills 54% of its Roche lobe in the inner binary. Thus, it is something of a competition as to whether star B, which is 12% more massive than Aa but fills far less of its Roche lobe, will start to transfer mass to the inner binary before Aa, which fills a larger fraction of its Roche lobe in the inner binary, starts mass transfer to Ab.

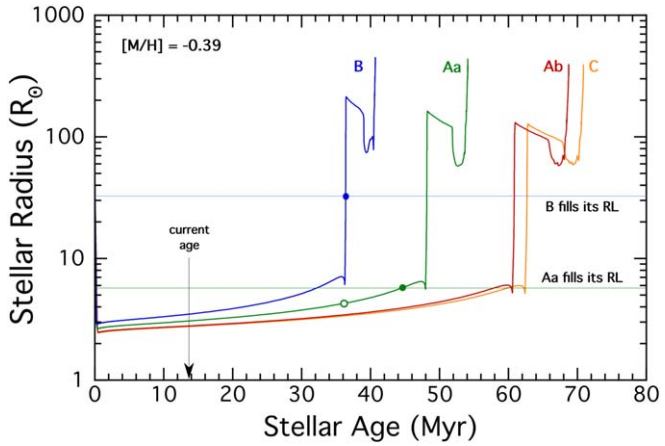

Figure 12. MIST radius evolution vs. time for the four stars in the TIC 290061484 system (the MIST tracks are from B. Paxton et al. 2011, 2013, 2015; A. Dotter 2016; J. Choi et al. 2016; and B. Paxton et al. 2018). The system is currently ∼14 Myr old (marked with an arrow). The most massive star, B, will ascend the giant branch at ∼36 Myr and begin to transfer mass to the inner binary (blue circle) shortly before star Aa fills its Roche lobe in the inner binary (∼45 Myr; green circle). What may happen during both of the mass transfer events is described in Section 6.8.

In Figure 12 we show the evolution of the stellar radii for all four stars as a function of time. Stars B and Aa ascend the giant branch at ages 36 and 48 Myr, respectively. However, after 36 Myr, when star B will overflow its Roche lobe in the outer orbit, star B will have an evolved radius of close to 4.2 $R_\odot$ and will be filling 75% of its Roche lobe while orbiting star Ab. It does appear that star B will be the first to overflow its Roche lobe and commence mass transfer onto the inner binary.

For the case of the tertiary overflowing its Roche lobe first, we look to the work of N. de Vries et al. (2014) for guidance, who modeled mass transfer in several much wider triples (including ξ Tau with $P_{\rm out} = 145$ days). The authors found that most of the mass transferred from the tertiary to the inner binary was ejected from the system without accreting onto the inner binary and that the ejected matter left the system from the L2 and L3 points. If, indeed, the tertiary star in TIC 290061484 evolves to fill its Roche lobe first and this is followed by the loss of its entire envelope, it will leave behind a ∼2 $M_\odot$ remnant core.

The inner binaries in the N. de Vries et al. (2014) calculations tended to shrink by some 5%–10% during the early part of the mass transfer process. In the context of TIC 290061484, this would drive the inner EB, with a current orbital period of 1.792 days, nearly into Roche lobe contact. Either the inner binary would be driven into actual Roche lobe contact by the episode of the tertiary transferring mass, or, within a few megayears thereafter, star Aa will naturally evolve to Roche lobe overflow via its nuclear evolution. Therefore, sooner or later, mass transfer within the inner binary will occur. Such mass transfer is likely to lead to the production of a merged star that is ∼12.9 $M_\odot$ and massive enough to undergo a Type II supernova.

However, before doing that, the merged inner binary will have expanded more than sufficiently to overflow its Roche lobe in the outer binary and engulf the tertiary star. The latter event would not unbind the envelope of the now merged 12.9 $M_\odot$ star whose envelope star B is entering, and the merged system would further evolve as a 15 $M_\odot$ star, leaving behind a neutron star.

This is a long, complex, and interesting road to the formation of an isolated neutron star!

Acknowledgments

This paper includes data collected by the TESS mission, which are publicly available from the Mikulski Archive for Space Telescopes (MAST). Funding for the TESS mission is provided by NASA's Science Mission directorate.

This research has made use of the Exoplanet Follow-up Observation Program website, which is operated by the California Institute of Technology, under contract with the National Aeronautics and Space Administration under the Exoplanet Exploration Program.

V.B.K., S.R., and B.P. acknowledge financial support of the NASA Citizen Science Seed Funding Program, grant No. 22-CSSFP22-0004. V.B.K. is grateful for financial support from NASA grant 80NSSC21K0631 and from NSF grant AST-2206814.

Resources supporting this work were provided by the NASA High-End Computing (HEC) Program through the NASA Center for Climate Simulation (NCCS) at Goddard Space Flight Center.

This work has made use of data from the European Space Agency (ESA) mission Gaia (https://www.cosmos.esa.int/gaia), processed by the Gaia Data Processing and Analysis Consortium (DPAC, https://www.cosmos.esa.int/web/gaia/dpac/consortium). Funding for the DPAC has been provided by national institutions, in particular the institutions participating in the Gaia Multilateral Agreement.

This project has received funding from the HUN-REN Hungarian Research Network. T.B. acknowledges the financial support of the Hungarian National Research, Development and Innovation Office—NKFIH grant K-147131. A.P. acknowledges the financial support of the Hungarian National Research, Development and Innovation Office—NKFIH grant K-138962.

Some of the observations in this paper made use of the High-Resolution Imaging instrument 'Alopeke and were obtained under Gemini LLP proposal No. GN/S-2021A-LP-105. 'Alopeke was funded by the NASA Exoplanet Exploration Program and built at the NASA Ames Research Center by Steve B. Howell, Nic Scott, Elliott P. Horch, and Emmett Quigley. 'Alopeke was mounted on the Gemini North telescope of the international Gemini Observatory, a program of NSF's OIR Lab, which is managed by the Association of Universities for Research in Astronomy (AURA) under a cooperative agreement with the National Science Foundation. on behalf of the Gemini partnership: the National Science Foundation (United States), National Research Council (Canada), Agencia Nacional de Investigación y Desarrollo (Chile), Ministerio de Ciencia, Tecnología e Innovación (Argentina), Ministério da Ciência, Tecnologia, Inovações e Comunicações (Brazil), and Korea Astronomy and Space Science Institute (Republic of Korea).

A portion of the research in this work was carried out at the Jet Propulsion Laboratory, California Institute of Technology, under a contract with the National Aeronautics and Space Administration (80NM0018D0004).

Facilities: Gaia, MAST, TESS, ATLAS, Gemini:Gillett.

Software: `Astropy` (Astropy Collaboration et al. 2013, 2018), `Eleanor` (A. D. Feinstein et al. 2019), `IPython` (F. Pérez & B. E. Granger 2007), `Keras` (F. Chollet 2015),

`LcTools` (A. R. Schmitt et al. 2019; A. Schmitt & A. Vanderburg 2021), `lightcurvefactory` (T. Borkovits et al. 2019a, 2020), `Lightkurve` (Lightkurve Collaboration et al. 2018), `Matplotlib` (J. D. Hunter 2007), `Mpi4py` (L. Dalcin et al. 2008), `NumPy` (C. R. Harris et al. 2020), `Pandas` (W. McKinney 2010), `Scikit-learn` (F. Pedregosa et al. 2011), `SciPy` (P. Virtanen et al. 2020), `Tensorflow` (M. Abadi et al. 2015), `Tess-point` (C. J. Burke et al. 2020).

Appendix A
Eclipse Times for the Inner 1.792-day Binary in TIC 290061484

Table 6 tabulates the midtimes of the regular binary eclipses of TIC 290061484 during the six sectors of TESS observations. Primary eclipses are designated by integer cycle numbers, while secondary eclipses have half-integer values.

Table 6
Eclipse Times for the Inner Binary in TIC 290061484, Extracted from the FITSH Light Curve

BJD −2,400,000	Cycle No.	Std. Dev. (days)	BJD −2,400,000	Cycle No.	Std. Dev. (days)	BJD −2,400,000	Cycle No.	Std. Dev. (days)	BJD −2,400,000	Cycle No.	Std. Dev. (days)
58712.12602	−0.5	0.00030	58754.25374	23.0	0.00026	59828.10505	622.0	0.00021	60356.96993	917.0	0.00033
58713.02277	0.0	0.00033	58755.15171	23.5	0.00030	59829.00452	622.5	0.00025	60357.86671	917.5	0.00040
58713.91819	0.5	0.00034	58756.05013	24.0	0.00036	59829.89724	623.0	0.00025	60358.76081	918.0	0.00037
58714.81379	1.0	0.00038	58756.94418	24.5	0.00035	59830.79770	623.5	0.00027	60359.66057	918.5	0.00030
58715.70989	1.5	0.00038	58757.84118	25.0	0.00032	59831.69366	624.0	0.00037	60360.55246	919.0	0.00033
58716.60597	2.0	0.00040	58758.73779	25.5	0.00039	59832.59484	624.5	0.00026	60361.44858	919.5	0.00032
58717.49993	2.5	0.00032	58759.63555	26.0	0.00030	59833.49147	625.0	0.00024	60362.34170	920.0	0.00029
58718.39713	3.0	0.00033	58760.53045	26.5	0.00040	59834.39058	625.5	0.00026	60363.23957	920.5	0.00033
58719.29179	3.5	0.00040	58761.42510	27.0	0.00037	59835.28514	626.0	0.00022	60364.13210	921.0	0.00030
58720.18866	4.0	0.00036	58762.32104	27.5	0.00054	59836.18435	626.5	0.00027	60365.02953	921.5	0.00031
58721.08454	4.5	0.00046	58763.21913	28.0	0.00060	59837.07734	627.0	0.00023	60365.92250	922.0	0.00027
58721.97972	5.0	0.00054	59797.63700	605.0	0.00026	59837.97882	627.5	0.00024	60366.82050	922.5	0.00031
58722.87403	5.5	0.00056	59798.53506	605.5	0.00032	59838.87225	628.0	0.00021	60367.71511	923.0	0.00074
58723.77121	6.0	0.00040	59799.42739	606.0	0.00030	59839.77318	628.5	0.00021	60368.61254	923.5	0.00032
58725.56272	7.0	0.00026	59800.32441	606.5	0.00031	59840.66742	629.0	0.00024	60369.50614	924.0	0.00033
58726.45751	7.5	0.00025	59801.21684	607.0	0.00030	59841.56638	629.5	0.00025	60370.40529	924.5	0.00036
58727.35651	8.0	0.00032	59802.11742	607.5	0.00034	59842.45776	630.0	0.00023	60371.30248	925.0	0.00035
58728.25469	8.5	0.00038	59803.00789	608.0	0.00033	59843.35765	630.5	0.00024	60372.20108	925.5	0.00037
58729.15509	9.0	0.00030	59803.90699	608.5	0.00036	59844.24903	631.0	0.00019	60373.09690	926.0	0.00034
58730.05272	9.5	0.00040	59804.80041	609.0	0.00036	59845.14801	631.5	0.00023	60373.99589	926.5	0.00036
58730.95139	10.0	0.00034	59805.69847	609.5	0.00036	59846.93883	632.5	0.00027	60374.89047	927.0	0.00029
58731.84611	10.5	0.00037	59806.59422	610.0	0.00029	59847.83099	633.0	0.00024	60375.78906	927.5	0.00031
58732.74441	11.0	0.00035	59807.49445	610.5	0.00036	59848.73015	633.5	0.00028	60376.68503	928.0	0.00027
58733.63745	11.5	0.00045	59808.39066	611.0	0.00024	59849.62115	634.0	0.00025	60377.58547	928.5	0.00029
58734.53561	12.0	0.00044	59809.29369	611.5	0.00026	59850.51989	634.5	0.00026	60379.38123	929.5	0.00028
58735.43090	12.5	0.00051	59811.08573	612.5	0.00023	59851.41039	635.0	0.00024	60380.27567	930.0	0.00027
58736.32880	13.0	0.00053	59811.98073	613.0	0.00021	59852.31166	635.5	0.00029	60381.17286	930.5	0.00029
58737.22428	13.5	0.00046	59812.87843	613.5	0.00021	60339.93283	907.5	0.00028	60382.06628	931.0	0.00025
58739.01538	14.5	0.00033	59813.77544	614.0	0.00026	60340.82678	908.0	0.00034	60382.96473	931.5	0.00028
58739.91179	15.0	0.00031	59814.67400	614.5	0.00029	60341.72206	908.5	0.00036	60383.85827	932.0	0.00034
58740.80702	15.5	0.00031	59815.56759	615.0	0.00025	60342.61705	909.0	0.00039	60384.75522	932.5	0.00035
58741.70402	16.0	0.00032	59816.46730	615.5	0.00029	60343.51497	909.5	0.00037	60385.64880	933.0	0.00033
58742.59803	16.5	0.00032	59817.36029	616.0	0.00024	60344.40906	910.0	0.00037	60386.54476	933.5	0.00033
58743.49538	17.0	0.00035	59818.26084	616.5	0.00029	60347.10142	911.5	0.00039	60387.43746	934.0	0.00032
58744.39082	17.5	0.00035	59819.15238	617.0	0.00030	60347.99960	912.0	0.00036	60388.33693	934.5	0.00071
58745.28569	18.0	0.00037	59820.05140	617.5	0.00031	60348.89766	912.5	0.00034	60389.22890	935.0	0.00032
58746.18120	18.5	0.00039	59820.94295	618.0	0.00024	60349.79219	913.0	0.00030	60390.12632	935.5	0.00030
58747.07682	19.0	0.00040	59821.84083	618.5	0.00034	60350.69039	913.5	0.00032	60391.01885	936.0	0.00033
58747.97316	19.5	0.00051	59822.73260	619.0	0.00029	60351.58626	914.0	0.00029	60391.91816	936.5	0.00034
58748.86842	20.0	0.00063	59823.63252	619.5	0.00028	60352.48570	914.5	0.00030	60392.81115	937.0	0.00027
58749.76556	20.5	0.00068	59825.42357	620.5	0.00029	60353.38337	915.0	0.00028	60393.70943	937.5	0.00027
58752.45519	22.0	0.00031	59826.31564	621.0	0.00022	60355.17814	916.0	0.00030	60394.60643	938.0	0.00024
58753.35304	22.5	0.00041	59827.21296	621.5	0.00025	60356.07552	916.5	0.00035	…	…	…

Appendix B
Population Synthesis of Compact Multiples

The toy model of A. Tokovinin & M. Moe (2020) not only simulates close binaries but also synthesizes compact triples and 2+1+1 quadruples while accounting for pre-MS mergers and disruptions as a result of dynamical instability. In their model, a brown dwarf companion fragments from the cool outer disk near $a = 200$ au, the expected seed mass and location of disk fragmentation (K. Kratter & G. Lodato 2016). The binary subsequently accretes from a circumbinary disk, driving the companion inward and increasing the mass ratio. Mass accretion and inward migration are treated in a stochastic manner, thereby producing a variety of multiple-star systems but with clear correlations, e.g., very close companions that underwent significant circumbinary accretion are more likely to be twins. In their model, the protostellar disk can fragment at random times and more than once during the main accretion phase, producing a rich diversity of binaries, triples, and quadruples.

To gain insight into the rarity of TIC 290061484, we run the population synthesis code of A. Tokovinin & M. Moe (2020) for 10^7 systems. Instead of assuming circular orbits, we draw outer components from a uniform eccentricity distribution across $e_{out} = 0.0$–0.8, consistent with the observed eccentricity distribution of companions beyond $P > 20$ days that have not been tidally circularized (A. Tokovinin 2014; M. Moe & R. Di Stefano 2017). We then impose the eccentricity-dependent stability criterion of Equation (1) and assume that outer components that migrate within this limit are ejected. We adopt the baseline solar-type model parameters from A. Tokovinin & M. Moe (2020), except that we set the input parameter that regulates the probability of disk fragmentation to $f_{bin} = 0.12$, which reproduces several observed properties of solar-type multiples. Specifically, this model yields a very close binary fraction within $P < 10$ days of 2%, a binary fraction within $P < 1{,}000$ days of 11%, and a triple fraction within $P_{out} < 10{,}000$ days of 0.3%.

In our simulation, the fractions of final systems with tertiaries below $P_{out} < 300$, 50, and 25 days are 7×10^{-5}, 6×10^{-6}, and 8×10^{-7}, respectively (see Figure 13). These results roughly match the observed ratios 59:9:1 in our current sample,[29] demonstrating that the A. Tokovinin & M. Moe (2020) toy model can approximately reproduce the tertiary period distribution of compact triples. About 0.3% of our simulated systems resulted in pre-MS mergers, and another 0.8% were triples that became dynamically disrupted. Indeed, the formation of an ultracompact triple is a delicate process. For every triple like TIC 290061484 that survived the hurdle of maintaining dynamical stability while migrating to $P_{out} < 25$ days, we expect $\sim 10^4$ triples to become dynamically unstable and disrupted during their formation process. More compact configurations are possible but substantially rarer. The tightest triple in our simulation of 10^7 systems has $P_{out} = 10$ days, consistent with our discussion in Section 6.5.

Our simulation predicts that there is one ultracompact triple like TIC 290061484 for every 1.3 million star systems. Accounting for the 10% probability that the tertiary is oriented across $i \approx 84°$–$96°$ to be detected as a triply eclipsing triple, then TIC 290061484 represents a unique object out of ~ 13 million systems. Given the finite sensitivity and selection biases of TESS, it is thus not surprising that it required searching through ~ 100 million stars and ~ 1 million EBs to find a rare ultracompact triple such as TIC 290061484.

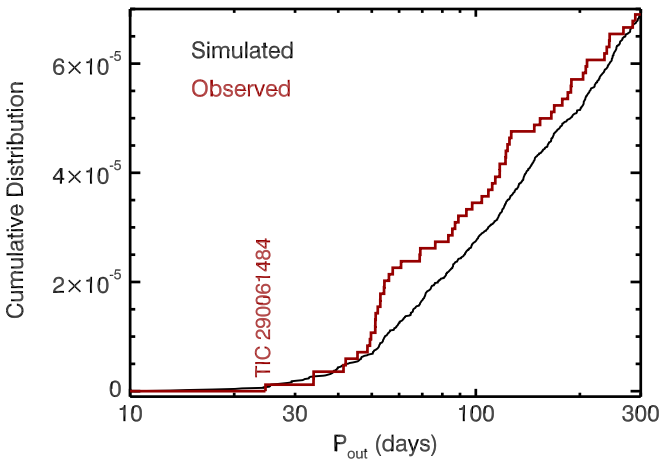

Figure 13. Cumulative distributions of tertiary periods P_{out} for the simulated population (black) and 59 observed compact triples with $P_{out} < 300$ days (red).

Our simulation also yielded 47 2+1+1 quadruples ($F_{quad} \approx 5 \times 10^{-6}$). The observed quadruple fraction of solar-type stars is considerably larger at 4% (A. Tokovinin 2014). Wider companions more likely derive from core fragmentation (A. Tokovinin 2017b), which is not encapsulated in the A. Tokovinin & M. Moe (2020) toy model of disk fragmentation, migration, and accretion. Indeed, the formation of the relatively common 2+2 quadruple architecture requires that the outer pair first formed via core fragmentation and then both of the resulting protostellar disks could subsequently fragment.

Of the six 2+1+1 quadruples in our simulation with $P_{quad} < 30{,}000$ days, all have extremely compact tertiaries with $P_{tert} < 300$ days. As discussed above, formation of very close binaries requires substantial migration in a massive disk/envelope, which is also more prone to fragment twice into a triple system. Similarly, the formation and migration of extremely compact triples with $P_{tert} < 50$ days require an even more massive disk/envelope, which is more likely to fragment three times into a 2+1+1 quadruple. It is therefore not surprising that TIC 290061484, the most compact triple yet discovered, also contains an additional component at $P \approx 3200$ days.

[29] We have added 15 additional triples to the set of 44 systems shown in Figure 10 with $P_{out} < 300$ days but without individually measured component masses. This brings the total number of compact triples in our sample to 59 objects.

ORCID iDs

V. B. Kostov https://orcid.org/0000-0001-9786-1031
S. A. Rappaport https://orcid.org/0000-0003-3182-5569
T. Borkovits https://orcid.org/0000-0002-8806-496X
B. P. Powell https://orcid.org/0000-0003-0501-2636
R. Gagliano https://orcid.org/0000-0002-5665-1879
S. B. Howell https://orcid.org/0000-0002-2532-2853
C. A. Clark https://orcid.org/0000-0002-2361-5812
M. H. Kristiansen https://orcid.org/0000-0002-2607-138X
A. Vanderburg https://orcid.org/0000-0001-7246-5438

References

Abadi, M., Agarwal, A., Barham, P., et al. 2015, TensorFlow: Large-Scale Machine Learning on Heterogeneous Systems, https://www.tensorflow.org/
Alonso, R., Deeg, H. J., Hoyer, S., et al. 2015, A&A, 584, L8
Applegate, J. H. 1992, ApJ, 385, 621

Astropy Collaboration, Price-Whelan, A. M., Sipőcz, B. M., et al. 2018, AJ, 156, 123
Astropy Collaboration, Robitaille, T. P., Tollerud, E. J., et al. 2013, A&A, 558, A33
Bailer-Jones, C. A. L., Rybizki, J., Fouesneau, M., Demleitner, M., & Andrae, R. 2021, AJ, 161, 147
Bate, M. R. 1998, ApJL, 508, L95
Bate, M. R. 2012, MNRAS, 419, 3115
Bate, M. R., Bonnell, I. A., & Bromm, V. 2002, MNRAS, 336, 705
Bate, M. R., Lodato, G., & Pringle, J. E. 2010, MNRAS, 401, 1505
Borkovits, T. 2022, Galax, 10, 9
Borkovits, T., Albrecht, S., Rappaport, S., et al. 2018, MNRAS, 478, 5135
Borkovits, T., Derekas, A., Kiss, L. L., et al. 2013, MNRAS, 428, 1656
Borkovits, T., Hajdu, T., Sztakovics, J., et al. 2016, MNRAS, 455, 4136
Borkovits, T., & Mitnyan, T. 2023, Univ, 9, 485
Borkovits, T., Mitnyan, T., Rappaport, S. A., et al. 2022a, MNRAS, 510, 1352
Borkovits, T., Rappaport, S., Hajdu, T., & Sztakovics, J. 2015, MNRAS, 448, 946
Borkovits, T., Rappaport, S., Kaye, T., et al. 2019a, MNRAS, 483, 1934
Borkovits, T., Rappaport, S. A., Hajdu, T., et al. 2020, MNRAS, 493, 5005
Borkovits, T., Rappaport, S. A., Toonen, S., et al. 2022b, MNRAS, 515, 3773
Borkovits, T., Sperauskas, J., Tokovinin, A., et al. 2019b, MNRAS, 487, 4631
Boss, A. P. 1986, ApJS, 62, 519
Burke, C. J., Levine, A., Fausnaugh, M., et al. 2020, TESS-Point: High precision TESS pointing tool, Astrophysics Source Code Library, ascl:2003.001
Carter, J. A., Fabrycky, D. C., Ragozzine, D., et al. 2011, Sci, 331, 562
Castelli, F., & Kurucz, R. L. 2003, in IAU Symp. 210, Modelling of Stellar Atmospheres, ed. N. Piskunov, W. W. Weiss, & D. F. Gray (San Francisco, CA: ASP), A20
Chambers, K. C., Magnier, E. A., Metcalfe, N., et al. 2016, arXiv:1612.05560
Choi, J., Dotter, A., Conroy, C., et al. 2016, ApJ, 823, 102
Chollet, F., et al. 2015, Keras, https://keras.io
Claret, A. 2023, A&A, 674, A67
Cutri, R. M., Wright, E. L., Conrow, T., et al. 2012, Explanatory Supplement to the WISE All-Sky Data Release Products
Dalcin, L., Paz, R., Storti, M., & DElia, J. 2008, JPDC, 68, 655
de Vries, N., Portegies Zwart, S., & Figueira, J. 2014, MNRAS, 438, 1909
Docobo, J. A., Piccotti, L., Abad, A., & Campo, P. P. 2021, AJ, 161, 43
Dotter, A. 2016, ApJS, 222, 8
Ebbighausen, E. G., & Struve, O. 1956, ApJ, 124, 507
Eisner, N. L., Johnston, C., Toonen, S., et al. 2022, MNRAS, 511, 4710
El-Badry, K., Rix, H.-W., Tian, H., Duchêne, G., & Moe, M. 2019, MNRAS, 489, 5822
Fabrycky, D., & Tremaine, S. 2007, ApJ, 669, 1298
Farris, B. D., Duffell, P., MacFadyen, A. I., & Haiman, Z. 2014, ApJ, 783, 134
Feinstein, A. D., Montet, B. T., Foreman-Mackey, D., et al. 2019, PASP, 131, 094502
Ford, E. B. 2005, AJ, 129, 1706
Gaia Collaboration, Brown, A. G. A., Vallenari, A., et al. 2021, A&A, 649, A1
Gaulme, P., Borkovits, T., Appourchaux, T., et al. 2022, A&A, 668, A173
Graham, M. J., Kulkarni, S. R., Bellm, E. C., et al. 2019, PASP, 131, 078001
Grether, D., & Lineweaver, C. H. 2006, ApJ, 640, 1051
Güver, T., & Özel, F. 2009, MNRAS, 400, 2050
Handler, G., Kurtz, D. W., Rappaport, S. A., et al. 2020, NatAs, 4, 684
Harris, C. R., Millman, K. J., van der Walt, S. J., et al. 2020, Natur, 585, 357
Heinze, A. N., Tonry, J. L., Denneau, L., et al. 2018, AJ, 156, 241
Howell, S. B., Everett, M. E., Sherry, W., Horch, E., & Ciardi, D. R. 2011, AJ, 142, 19
Hunter, J. D. 2007, CSE, 9, 90
Innes, R. T. A. 1917, CiUO, 40, 331
Kervella, P., Thévenin, F., & Lovis, C. 2017, A&A, 598, L7
Kiseleva, L. G., Eggleton, P. P., & Mikkola, S. 1998, MNRAS, 300, 292
Kochanek, C. S., Shappee, B. J., Stanek, K. Z., et al. 2017, PASP, 129, 104502
Kostov, V. B., Powell, B. P., Rappaport, S. A., et al. 2022, ApJS, 259, 66
Kostov, V. B., Powell, B. P., Rappaport, S. A., et al. 2024, MNRAS, 527, 3995
Kovács, G., Zucker, S., & Mazeh, T. 2002, A&A, 391, 369
Kratter, K., & Lodato, G. 2016, ARA&A, 54, 271
Kristiansen, M. H. K., Rappaport, S. A., Vanderburg, A. M., et al. 2022, PASP, 134, 074401
Lightkurve Collaboration, Cardoso, J. V. d. M., Hedges, C., et al. 2018, Lightkurve: Kepler and TESS time series analysis in Python, Astrophysics Source Code Library, ascl:1812.013
Mardling, R. A., & Aarseth, S. J. 2001, MNRAS, 321, 398
McKinney, W. 2010, in Proc. of the 9th Python in Science Conf., ed. S. van der Walt & J. Millman, 56
Mikkola, S. 2008, in The Cambridge N-Body Lectures, ed. S. J. Aarseth, C. A. Tout, & R. A. Mardling, Vol. 760 (Berlin: Springer), 31
Miller, N. J., Maxted, P. F. L., & Smalley, B. 2020, MNRAS, 497, 2899
Mitnyan, T., Borkovits, T., Rappaport, S. A., Pál, A., & Maxted, P. F. L. 2020, MNRAS, 498, 6034
Moe, M., & Di Stefano, R. 2017, ApJS, 230, 15
Moe, M., & Kratter, K. M. 2018, ApJ, 854, 44
Moharana, A., Hełminiak, K. G., Marcadon, F., et al. 2024, arXiv:2405.12136
Nanouris, N., Kalimeris, A., Antonopoulou, E., & Rovithis-Livaniou, H. 2011, A&A, 535, A126
Nanouris, N., Kalimeris, A., Antonopoulou, E., & Rovithis-Livaniou, H. 2015, A&A, 575, A64
Naoz, S. 2016, ARA&A, 54, 441
Nguyen, C. T., Costa, G., Girardi, L., et al. 2022, A&A, 665, A126
Offner, S. S. R., Moe, M., Kratter, K. M., et al. 2023, in ASP Conf. Ser. 534, Protostars and Planets VII, 534, ed. S. Inutsuka et al. (San Francisco, CA: ASP), 275
Orosz, J. A. 2023, Univ, 9, 505
Pal, A. 2012, MNRAS, 421, 1825
Paxton, B., Bildsten, L., Dotter, A., et al. 2011, ApJS, 192, 3
Paxton, B., Cantiello, M., Arras, P., et al. 2013, ApJS, 208, 4
Paxton, B., Marchant, P., Schwab, J., et al. 2015, ApJS, 220, 15
Paxton, B., Schwab, J., Bauer, E. B., et al. 2018, ApJS, 234, 34
Pedregosa, F., Varoquaux, G., Gramfort, A., et al. 2011, JMLR, 12, 2825
Pérez, F., & Granger, B. E. 2007, CSE, 9, 21
Powell, B. 2022, TESS FFI-Based Light Curves from the GSFC Team ("GSFC-ELEANOR-LITE"), STScI/MAST, doi:10.17909/J2YT-T417
Powell, B. P., Kostov, V. B., Rappaport, S. A., et al. 2021a, AJ, 161, 162
Powell, B. P., Kostov, V. B., Rappaport, S. A., et al. 2021b, AJ, 162, 299
Powell, B. P., Kruse, E., Montet, B. T., et al. 2022a, RNAAS, 6, 111
Powell, B. P., Rappaport, S. A., Borkovits, T., et al. 2022b, ApJ, 938, 133
Pribulla, T., Borkovits, T., Jayaraman, R., et al. 2023, MNRAS, 524, 4220
Raghavan, D., McAlister, H. A., Henry, T. J., et al. 2010, ApJS, 190, 1
Rappaport, S., Deck, K., Levine, A., et al. 2013, ApJ, 768, 33
Rappaport, S. A., Borkovits, T., Gagliano, R., et al. 2022, MNRAS, 513, 4341
Rappaport, S. A., Borkovits, T., Gagliano, R., et al. 2023, MNRAS, 521, 558
Rappaport, S. A., Borkovits, T., Mitnyan, T., et al. 2024, A&A, 686, A27
Rein, H., & Liu, S.-F. 2012, A&A, 537, A128
Schmitt, A., & Vanderburg, A. 2021, arXiv:2103.10285
Schmitt, A. R., Hartman, J. D., & Kipping, D. M. 2019, arXiv:1910.08034
Scott, N. J., Howell, S. B., Gnilka, C. L., et al. 2021, FrASS, 8, 138
Skrutskie, M. F., Cutri, R. M., Stiening, R., et al. 2006, AJ, 131, 1163
Stassun, K. G., Oelkers, R. J., Pepper, J., et al. 2018, AJ, 156, 102
Stassun, K. G., & Torres, G. 2016, AJ, 152, 180
Tamayo, D., Rein, H., Shi, P., & Hernandez, D. M. 2020, MNRAS, 491, 2885
Tokovinin, A. 2014, AJ, 147, 87
Tokovinin, A. 2017a, ApJ, 844, 103
Tokovinin, A. 2017b, MNRAS, 468, 3461
Tokovinin, A. 2021, Univ, 7, 352
Tokovinin, A., & Moe, M. 2020, MNRAS, 491, 5158
Tokovinin, A., Thomas, S., Sterzik, M., & Udry, S. 2006, A&A, 450, 681
Tokovinin, A. A. 2000, A&A, 360, 997
Valtonen, M., & Karttunen, H. 2006, The Three-Body Problem (Cambridge: Cambridge Univ. Press)
Virtanen, P., Gommers, R., Oliphant, T. E., et al. 2020, NatMe, 17, 261
Young, M. D., & Clarke, C. J. 2015, MNRAS, 452, 3085